Supporting Information

Substrate-independent and Antisolvent-free Fabrication Method of Tin Perovskite Films via Imidazole-complexed Intermediates

Fuyuki Harata,[1] Ryuji Kaneko,[1, 2] Shuaifeng Hu,[1] Noboru Ohashi,[1] Tomoya Nakamura,[1]* Minh Anh Truong,[1] Richard Murdey,[1] and Atsushi Wakamiya[1]*

[1]Institute for Chemical Research, Kyoto University, Gokasho, Uji, Kyoto 611-0011, Japan

[2]EneCoat Technologies Co., Ltd., 43-1, Satoyashiki, Kumiyama-cho, Kuse-gun, Kyoto 613-0031, Japan

*E-mail: tomoya@scl.kyoto-u.ac.jp, wakamiya@scl.kyoto-u.ac.jp

Materials:

Formamidinium hydroiodide (FAI, 99.99%), formamidinium hydrobromide (FABr, 99.99%) bathocuproine (BCP, 99%, purified by sublimation), 1-vinylimidazole (>98.0%), 1-ethylimidazole (>98.0%), 1,2-dimethylimidazole (>98.0%), MeO-2PACz (>98.0%), and titanium(IV) diisopropoxide bis(acetylacetonate) (75 wt% in isopropanol) were purchased from Tokyo Chemical Industry Co., Ltd. (TCI). Tin(II) fluoride (SnF_2, 99%), tin(II) iodide (SnI_2, beads, 99.99%, trace metals basis), ethane-1,2-diammonium iodide (ethylenediammonium diiodide, $EDAI_2$, 98%), phenethylammonium iodide (PEAI, 98%), and tin powder (<45 μm particle size, 99.8%, trace metals basis) were purchased from Sigma-Aldrich Co., Ltd. (Sigma-Aldrich). Poly(3,4-ethylenedioxythiophene):poly (styrene sulfonate) (PEDOT:PSS) aqueous solution (Clevios PVP AI 4083) was purchased from Heraeus Co., Ltd. Fullerene C_{60} (sublimed, 99.99%) was purchased from ATR Company. Phenyl-C_{61}-butyric acid methyl ester (PCBM, >99.0%), and Indene-C_{60} bisadduct (ICBA, >99.0%) were purchased from Ossila. Titanium(IV) tetrachloride ($TiCl_4$, 99.0%), dehydrated dimethyl sulfoxide (DMSO, super dehydrated), ethanol (EtOH, super dehydrated), and 2-propanol (IPA, super dehydrated) were purchased from FUJIFILM Wako Pure Chemical Co., Ltd. Dimethylformamide (DMF), and chlorobenzene were purchased from Kanto Chemical. Co., Inc. All of these solvents were degassed by Ar gas bubbling for 30 min and further dried with molecular sieves (3 Å or 4 Å) in an Ar-filled glove box (H_2O, O_2 <0.1 ppm) before use. All other purchased materials were used as received, without further purification, unless otherwise noted.

Perovskite layer fabrication:

Antisolvent method:

The perovskite film preparation was conducted in an Ar-filled glove box (H_2O, O_2 < 0.1 ppm). 1.0 M $EDA_{0.01}FA_{0.98}SnI_3$ perovskite solution was prepared by dissolving FAI (168.5 mg, 0.98 mmol), $EDAI_2$ (3.2 mg, 0.01 mmol), SnI_2 (372.5 mg, 1.00 mmol), SnF_2 (15.7 mg, 0.10 mmol), and tin powder (20 mg) in 1.0 mL DMSO. The precursor solution was stirred at 45 °C for 1 hour and then filtered through a 0.20 μm PTFE filter before spin-coating. 150 μL of the precursor solution was spin-coated at 5000 rpm for 60 s with an acceleration of 1000 rpm s^{-1}. 300 μL of chlorobenzene (preheated to 65 °C) was dripped onto the surface of the spinning substrate at 62 s during the spin-coating step. The substrate was immediately annealed on a hot plate at 65 °C for over 10 minutes and then at 100 °C for 10 minutes.

Vacuum-quenching method:

The perovskite film preparation was conducted in a N_2-filled glove box (H_2O, O_2 < 0.1 ppm). 0.7 M $EDA_{0.01}FA_{0.98}SnI_3$ perovskite solution was prepared by dissolving FAI (118.0 mg, 0.69 mmol), $EDAI_2$ (2.2 mg, 0.007 mmol), SnI_2 (260.8 mg, 0.70 mmol), SnF_2 (11.0 mg, 0.07 mmol), 1-vinylimidazole (63.4 μL, 0.70 mmol), and tin powder (20 mg) in 1.0 mL DMF. After being stirred at 45 °C for 1 h, the solution was cooled down to 20 °C and stirred overnight. The solution was filtered through a 0.20 μm PTFE filter. A liquid film was formed by adding the perovskite precursor solution and spinning the substrate at 3000 rpm for 3 s with an acceleration of 3000 rpm s^{-1}. The substrate was immediately transferred to a vacuum box and dried under a reduced pressure of less than 2 hPa. The optimized drying times were 3 minutes for a rotary pump (GCD-136X, ULVAC, Inc.) and 1 minute for a screw pump (VACUU PURE 10C, VACUUBRAND, Inc.). The vacuum box was then refilled with N_2. The films were annealed on a 1.5 mm high rubber bar placed on a hot plate at 100 °C for 5 min, and then directly on the hot plate at 100 °C for another 15 min.

Device fabrication:

Glass/ITO substrates (10 Ω sq^{-1}, Geomatec Co., Ltd.) were etched with zinc powder and HCl (6 M in de-ionized water). Then, the substrates were consecutively cleaned with water, acetone, a detergent solution (Semico Clean 56, Furuuchi Chemical), water, and 2-propanol using a 15-minute ultrasonic bath, followed by drying with an air gun. Finally, the organic residues on substrates were removed with nitrogen plasma (JP-100HA, Aqa Co., Ltd.). For devices using PEDOT:PSS as a hole-transporting layer, the PEDOT:PSS aqueous dispersion was filtered through a 0.45 μm PVDF filter and then spin-coated on the ITO surface at 500 rpm for 10 s and 5000 rpm for 30 s. The samples were then annealed at 140 °C for 20 min. The substrates were transferred to an Ar-filled glove box (H_2O, O_2 < 0.1 ppm) and annealed at 140 °C for an additional 20 min. For the devices using MeO-2PACz as a hole-transporting material, MeO-2PACz (1.0 mmol L^{-1} in anhydrous ethanol) was deposited by spin-coating (3000 rpm for 30 s, 600 rpm s^{-1} acceleration), followed by heating on a hot plate at 100 °C for 10 min.[1] The perovskite layer was fabricated on top of the hole-transporting materials following the procedure mentioned above. For $EDAI_2$ surface treatment, the samples were transferred under an inert atmosphere to a vacuum deposition chamber, where 1.0 nm of $EDAI_2$ (deposition rate 0.01 nm s^{-1}) was deposited by thermal evaporation. After thermal evaporation, the samples were moved to an N_2-filled glove box and annealed at 100 °C for 10 min.[2] For PCBM/ICBA surface treatment, PCBM/ICBA mixed solution (1.0 mg/mL, 4:1 w/w) in chlorobenzene was deposited by spin-coating (3000 rpm for 30 s, 600 rpm s^{-1} acceleration), followed by annealing at 70 °C for 10 min.[3] Then, 20 nm of C_{60} (0.01 nm s^{-1}) and 8 nm of BCP (0.01 nm s^{-1}) were deposited by thermal evaporation. Finally, 80 nm of Ag was deposited through a shadow mask to form the metal electrode. The deposition rate for Ag was set at 0.003 nm s^{-1} until the thickness reached 5 nm, then increased to 0.01 nm s^{-1} until 20 nm, and finally to 0.1 nm s^{-1} until the target thickness was achieved. The device area was approximately 0.14 mm^2.

Slot-die coating of tin perovskite films was carried out using a New Takudai M-150 (Die-Gate Co., Ltd.) and a shim 15 cm wide and 50 μm thick. The above-mentioned perovskite precursor solution was coated onto 15 cm × 17 cm substrates with an effective gap of 100 μm and a velocity of 10 mm/s. The thickness of the wet film was 4 μm.

For the fabrication of the solar module, the module pattern processing (P1, shown in Figure S30) was performed by laser scribing (LPM-300, Mitsuboshi Diamond Industrial Co., Ltd.). The pulse width, wavelength, and power of the laser were <15 ps, 532 nm, and 0.1–0.3 W, respectively. Patterning was performed in a nitrogen atmosphere. The module pattern processing (P2 and P3) was performed by mechanical scribing (MPV250-AT, Mitsuboshi Diamond Industrial Co., Ltd.) in an N_2-filled glove box (H_2O, $O_2 < 1$ ppm). The pattern widths of P1, P2, and P3 were 80 μm, 150 μm, and 80 μm, respectively. The geometric fill factor was 95%.

For the fabrication of glass/FTO/TiO_2 substates, glass/FTO substrates (10 Ω sq^{-1}, Asahi Glass Co., Ltd.) were etched with zinc powder and HCl (6 M in de-ionized water). Then, the substrates were consecutively cleaned with water, acetone, a detergent solution (Semico Clean 56, Furuuchi Chemical), water, and 2-propanol using a 15-minute ultrasonic bath, followed by drying with an air gun. Finally, the organic residues on substrates were removed with nitrogen plasma (JP-100HA, Aqa Co., Ltd.). To deposit the compact-TiO_2 layer, the FTO substrate was covered with stainless steel masks and heated on a hot plate at 450 °C. A 0.05 M solution of titanium diisopropoxide bis(acetylacetonate) (75 wt% in 2-propanol) in ethanol was sprayed over the substrates at a sweep speed of approximately 20 cm s^{-1} from a distance of 30 cm. After six spray cycles, spaced 3 minutes apart, the substrates were cooled to room temperature. The substrates were then immersed in a 0.77 wt% aqueous solution of $TiCl_4$ at 70 °C for 30 min, followed by rinsing twice with distilled water. They were then sintered at 500°C for 20 minutes.

Characterization:

Photocurrent-voltage (*J*–*V*) measurements for perovskite solar cells were performed in a nitrogen-filled glovebox (O2 < 1 ppm) using an OTENTO-SUN-P1G (BUNKOUKEIKI Co., Ltd.) and a Keithley 2400. The light intensity of the illumination source was adjusted using a standard BS520 silicon photodiode. During measurement, the devices were covered with shadowed masks with an area of 0.0985 cm^2. External quantum efficiency (EQE) and internal quantum efficiency (IQE) spectra were measured by an SMO-250III system equipped with an SM-250 diffuse reflection unit (BUNKOUKEIKI Co., Ltd.). The light intensity of the illumination source was adjusted using a standard SiPD S1337-1010BQ silicon photodiode.

Thin film X-ray diffraction (XRD) measurements were performed on a Rigaku SmartLab equipped with a hybrid pixel array detector HyPix-3000. Perovskite films were deposited on the surface of PEDOT:PSS with glass/ITO as substrates. The samples were kept in an argon-filled airtight specimen holder during XRD measurements. All samples were scanned with 2θ ranging from 5° to 50° in 0.02° increments. The power supply was operated at 300 mA and 40 kV.

Scanning electron microscopy (SEM) observations were performed using an SU-8010 or SU-8600 (Hitachi High-Technologies Co.) instrument.

The ^{1}H and ^{119}Sn NMR measurements were carried out with a Bruker Avance-400 spectrometer (400 MHz for ^{1}H NMR, 149 MHz for ^{119}Sn NMR). The chemical shifts in ^{1}H NMR spectra were reported in ppm relative to the residual proton signal in DMSO-d_6 ($\delta = 2.50$ ppm). For ^{119}Sn spectra, tetramethyltin ($\delta = 0.00$ ppm) was used as an external standard. NMR spectra were processed using MestReNova version 14.0.0.

Single-crystal X-ray diffraction data were recorded on a Rigaku single-crystal CCD X-ray diffractometer (XtaLAB Synergy-i) with Mo Kα radiation (λ = 0.71073Å) and a graphite monochromator. The measurements were carried out at 100 K. The structure was solved using direct methods (SHELXT-2018/2) and refined by full-matrix least-squares on F^2 (SHELXL-2018/1)[4]. All hydrogen atoms were placed using the AFIX instructions. Crystallographic data have been deposited with the Cambridge Crystallographic Data Center as supplementary publication no. CCDC-2413228 ([SnI_2–(1-vinylimidazole)]), CCDC-2413229 ([SnI_2–(1-ethylimidazole)$_2$]), and CCDC-2413230 ([SnI_2–(1,2-dimethylimidazole)$_2$]). These data can be obtained free of charge from The Cambridge Crystallographic Data Centre via www.ccdc.cam.ac.uk/data_request/cif.

For the PL (photoluminescence) and time-resolved photoluminescence (TRPL) measurements, the samples were excited from the film surface side using a picosecond pulsed light with a wavelength of 688 nm (Advanced Laser Diode System) and an excitation fluence of 100 nJ cm^{-2}. PL spectra were recorded using a liquid nitrogen-cooled indium gallium arsenide (InGaAs) array equipped with an Acton SP-2300i monochromator (Princeton

Instruments). The TRPL signals were recorded using an avalanche photodiode (ID Quantique) and a time-correlated single photon counting board (PicoQuant). The PL lifetimes were obtained by fitting the PL decay curve with an exponential function. During the measurements, the samples were kept in an N_2-filled metallic box with quartz windows.

For the photoluminescence quantum yield (PLQY) measurements, samples were placed inside an integrating sphere and excited from the substrate side with a 660 nm continuous wave laser (Integrated optics). The resulting PL signal was collected with a spectrometer (Thorlabs CCS175). Quasi-Fermi level splitting (QFLS) was calculated according to the following equation:[5]

$$\mathrm{QFLS} = \frac{k_\mathrm{B}T}{q}\ln\left(\mathrm{PLQY}\frac{J_\mathrm{sc,int}}{J_\mathrm{s,rad}}\right)$$

where, k_B is the Boltzmann constant, q is the elementary charge, $J_\mathrm{sc,int}$ is the short-circuit current density, and $J_\mathrm{s,rad}$ is the radiative recombination current in the dark.

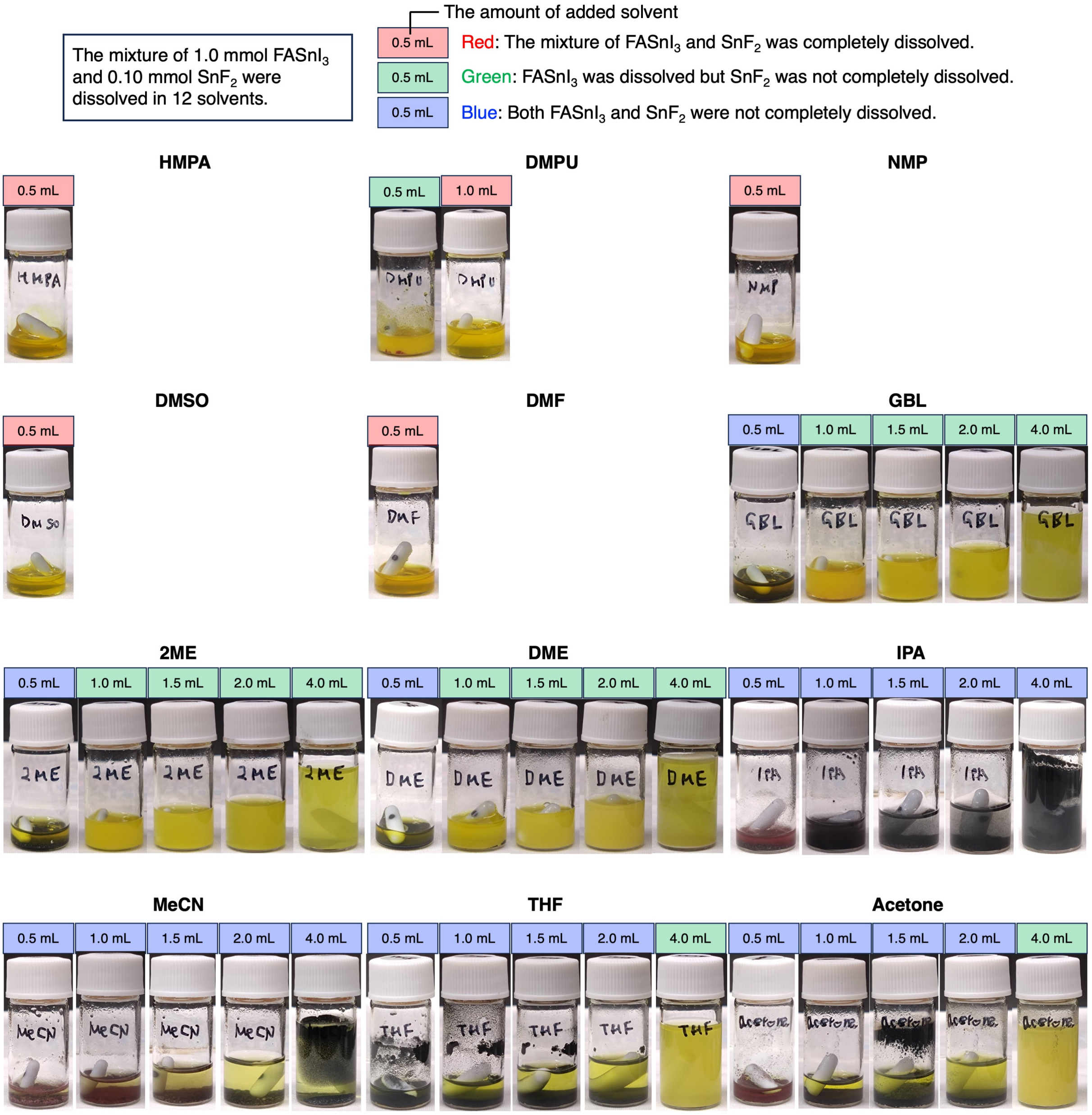

Figure S1. Solubility test of FASnI$_3$ with 10 mol% SnF$_2$ in 12 solvents. The mixture of 1.0 mmol FASnI$_3$ and 0.1 mmol SnF$_2$ in various solvent amounts was stirred for at least 15 minutes at room temperature. Black precipitates correspond to undissolved tin perovskite, whereas white precipitates correspond to undissolved SnF$_2$.

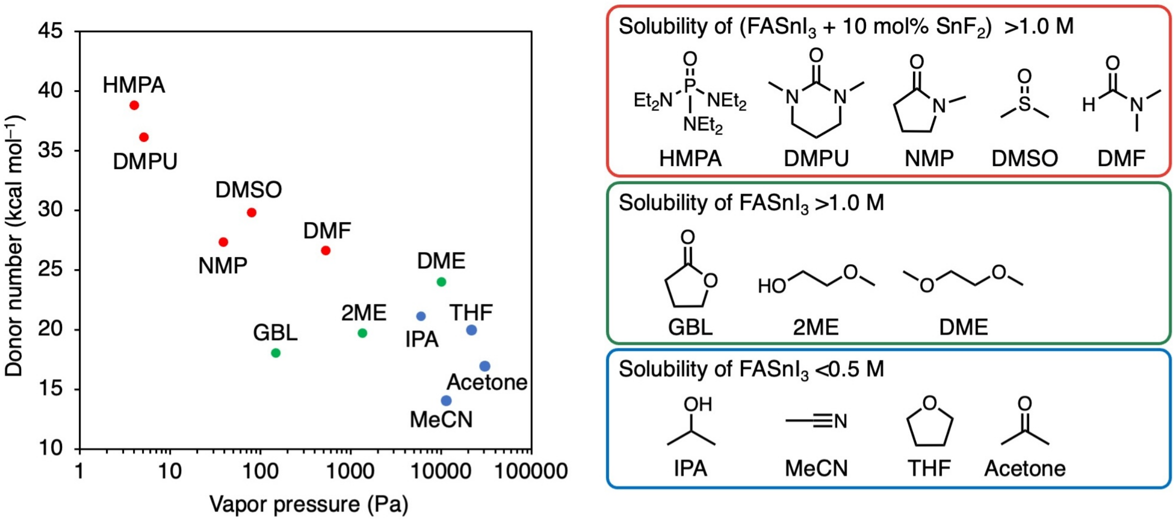

Figure S2. Gutmann donor number[6] versus the vapor pressure of 12 solvents.[7] The solvents indicated by the red dots dissolved $FASnI_3$ with 10 mol% SnF_2 above 1.0 M. The solvents indicated by the green dots dissolve more than 1.0 M of $FASnI_3$ without SnF_2, while the solubility of $FASnI_3$ with 10 mol% SnF_2 is less than 0.5 M. The solvents indicated by the blue dots are not suitable as solvents because the solubility of $FASnI_3$ without SnF_2 is below 0.5 M.

DFT calculations

Density functional theory (DFT) calculations were performed with the Gaussian 16 software package.[8] The geometry optimizations were conducted at the B97D3/def2-TZVP level of theory, and the frequency calculations were conducted at the PW6B95D3/def2-TZVP level of theory.[9, 10] The solvent effect was taken into account by the polarizable continuum model (PCM) of dimethylformamide.

Enthalpy change resulting from the formation of a 1:1 complex of additives with SnI_2 is calculated in eq1:

$$\Delta H(\mathrm{SnI_2{-}additives}) = H(\mathrm{1{:}1\ complex}) - H(\mathrm{additives}) - H(\mathrm{SnI_2}) \qquad (1)$$

where the terms H(1:1 complex), H(additives), and H(SnI_2) represent the calculated enthalpy of a SnI_2–additive complex, an additive, and a SnI_2 molecule in DMF matrix respectively.

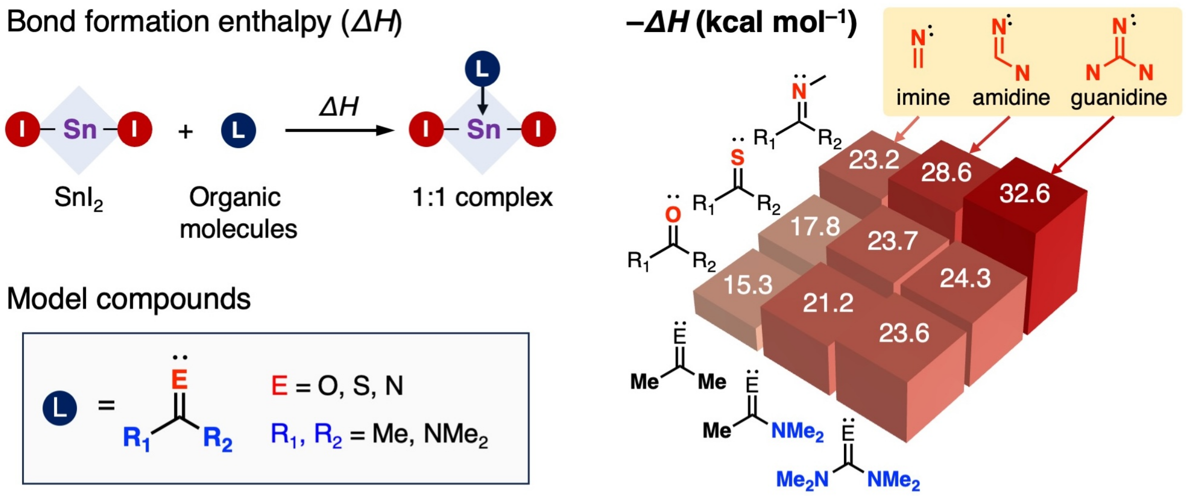

Figure S3. Chemical structures of 9 model compounds and calculated ΔH. The geometry optimizations were conducted at the B97D3/def2-TZVP level of theory, and the frequency calculations were performed at the PW6B95D3/def2-TZVP level of theory.

Table S1. pKa of representative Lewis base molecules with a nitrogen coordinating group.[11]

Molecules	pKa of conjugate acid
Pyridine	5.18
Vinylimidazole	6.07
Imidazole	6.95
Ethylimidazole	7.26
Dimethylimidazole	8.21
Formamidine	**11.5**
Tetramethylguanidine	13.6

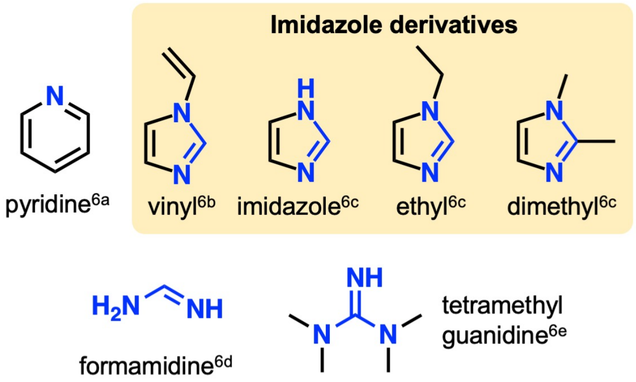

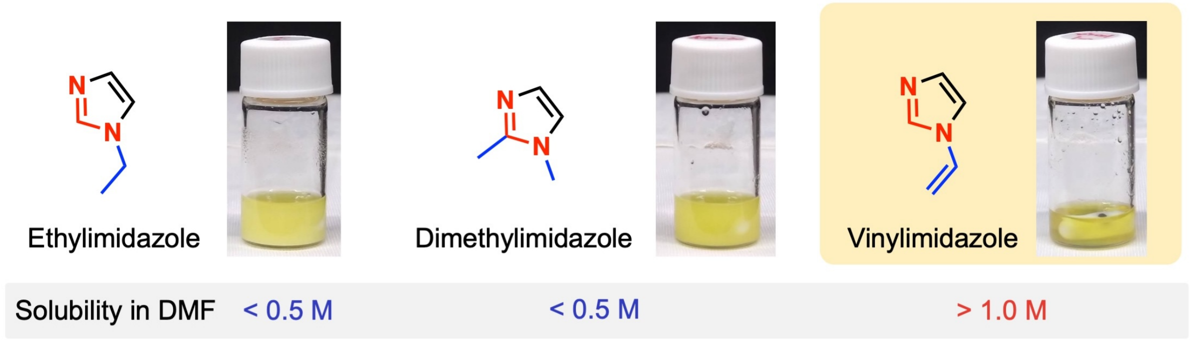

Figure S4. Solubility test of $FASnI_3$ with 100 mol% 1-ethylimidazole, 1,2-dimethylimidazole, and 1-vinylimidazole in DMF solvent. The mixture of 1.0 mmol $FASnI_3$ and 1.0 mmol imidazole derivatives in DMF was stirred for more than 30 minutes at room temperature.

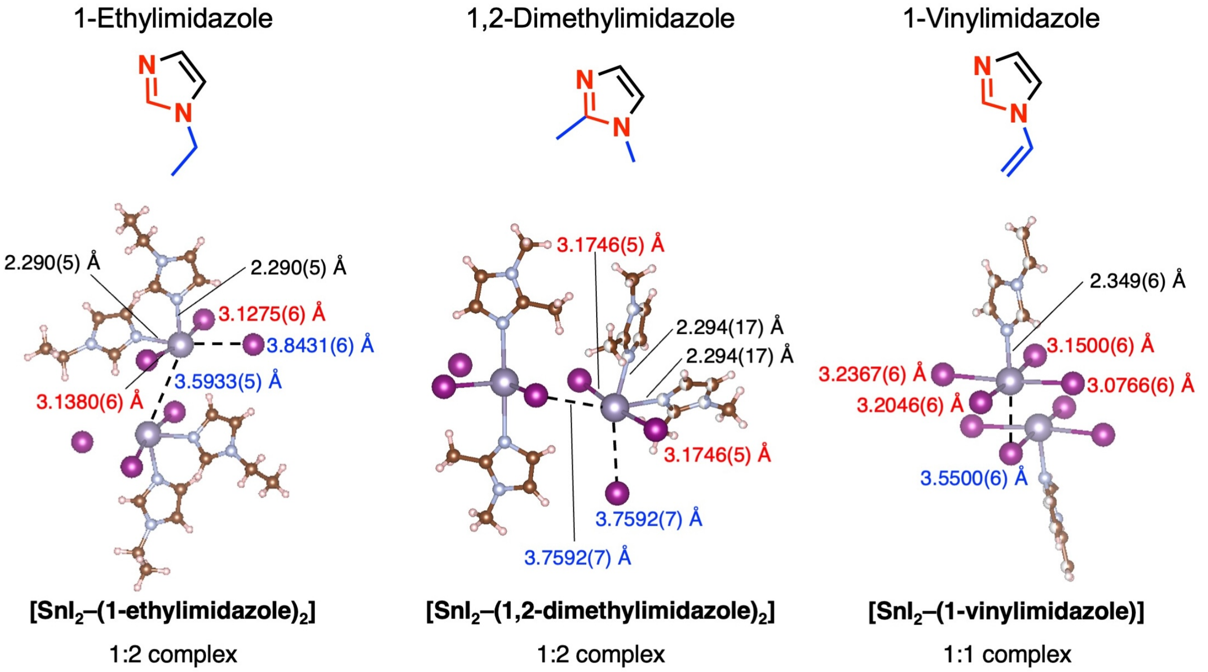

1-Ethylimidazole

1,2-Dimethylimidazole

1-Vinylimidazole

[SnI_2–(1-ethylimidazole)$_2$]
1:2 complex

[SnI_2–(1,2-dimethylimidazole)$_2$]
1:2 complex

[SnI_2–(1-vinylimidazole)]
1:1 complex

Figure S5. X-ray single-crystal structures of [SnI_2–(1-ethylimidazole)]$_2$ at 298 K, [SnI_2–(1,2-dimethylimidazole)]$_2$ at 100 K, and [SnI_2–(1-vinylimidazole)] at 298 K. Crystal and structural refinement data were summarized in Table S2.

Table S2. Crystal and structural refinement data of [SnI_2–(1-vinylimidazole)], [SnI_2–(1-ethylimidazole)$]_2$ at 298 K, and [SnI_2–(1,2-dimethylimidazole)$]_2$ at 100 K, and [SnI_2–(1-vinylimidazole)] at 298 K.

	[SnI_2–(1-ethylimidazole)$]_2$	[SnI_2–(1,2-dimethylimidazole)$]_2$	[SnI_2–(1-vinylimidazole)]
Crystal system	Monoclinic	Trigonal	Monoclinic
Space group	$P2_1/c$	$P3_121$	$P2_1/c$
Unit cell a [Å]	14.4816(5)	10.26030(10)	12.0207(3)
Unit cell b [Å]	13.3963(5)	10.26030(10)	4.42480(10)
Unit cell c [Å]	8.3729(3)	25.3658(4)	19.5033(4)
Unit cell α [°]	90	90	90
Unit cell β [°]	94.575(3)	90	91.891(2)
Unit cell γ [°]	90	120	90
Volume [Å^3]	1619.17(10)	2312.59(6)	1036.80(4)
Z	4	6	4
Density (calc)	2.317	2.433	2.989
Independent reflections	3306 [$R_{int} = 0.0372$]	3151 [$R_{int} = 0.0736$]	2381 [$R_{int} = 0.0415$]
Goodness-of-fit	1.023	1.169	1.201
Final R indices [$I > 2\sigma(I)$]	$R_{obs} = 0.0323$ $wR_{obs} = 0.0759$	$R_{obs} = 0.0224$ $wR_{obs} = 0.0461$	$R_{obs} = 0.0294$ $wR_{obs} = 0.0737$
R indices [all data]	$R_{all} = 0.0448$ $wR_{all} = 0.0826$	$R_{all} = 0.0226$ $wR_{all} = 0.0462$	$R_{all} = 0.0331$ $wR_{all} = 0.0757$

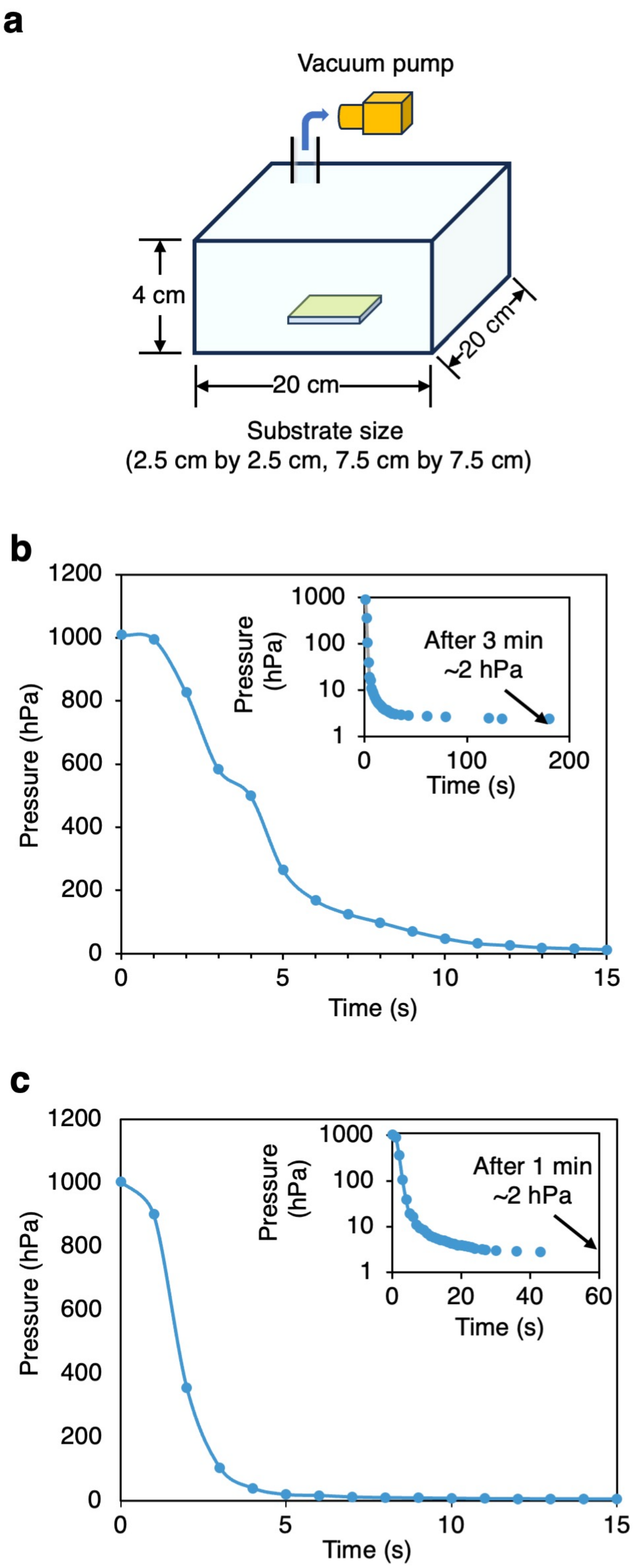

Figure S6. (a) Setting for vacuum-quenching. For 15 by 17 cm^2 substrates, a larger box (26 by 26 by 10 cm^3) was used. The pressure change inside the vacuum chamber (b) when using a rotary pump (GCD-136X, ULVAC, Inc.) and (c) when using a screw pump (VACUU PURE 10C, VACUUBRAND, Inc.)

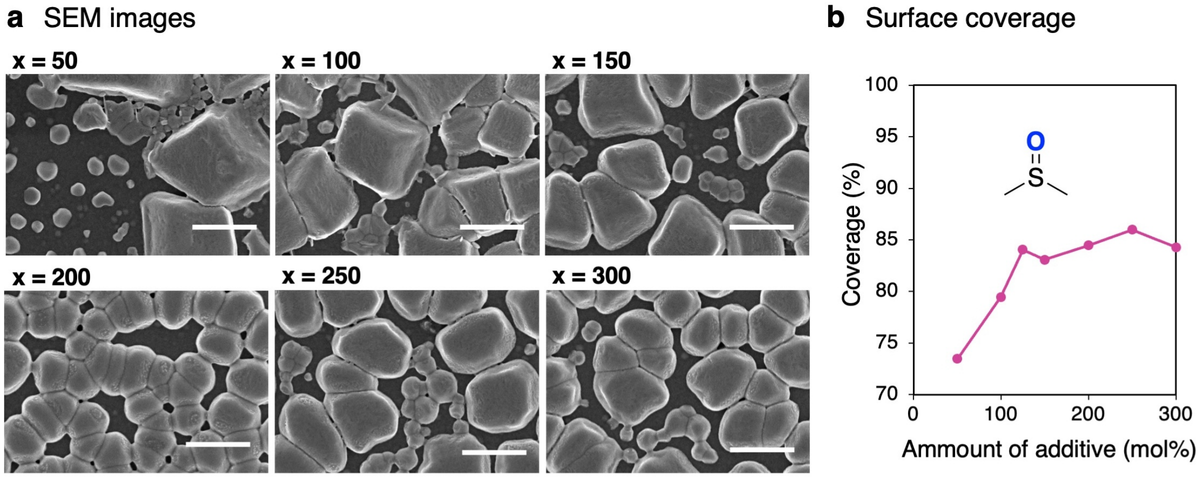

Figure S7. (a) SEM images of tin perovskite thin film fabricated by the vacuum quenching method with different amounts of DMSO. The scale bar represents 1.0 μm. (b) Surface coverage changes with the amount of additive. Even after increasing the DMSO content to 300 mol%, the substrate coverage remained at approximately 85%.

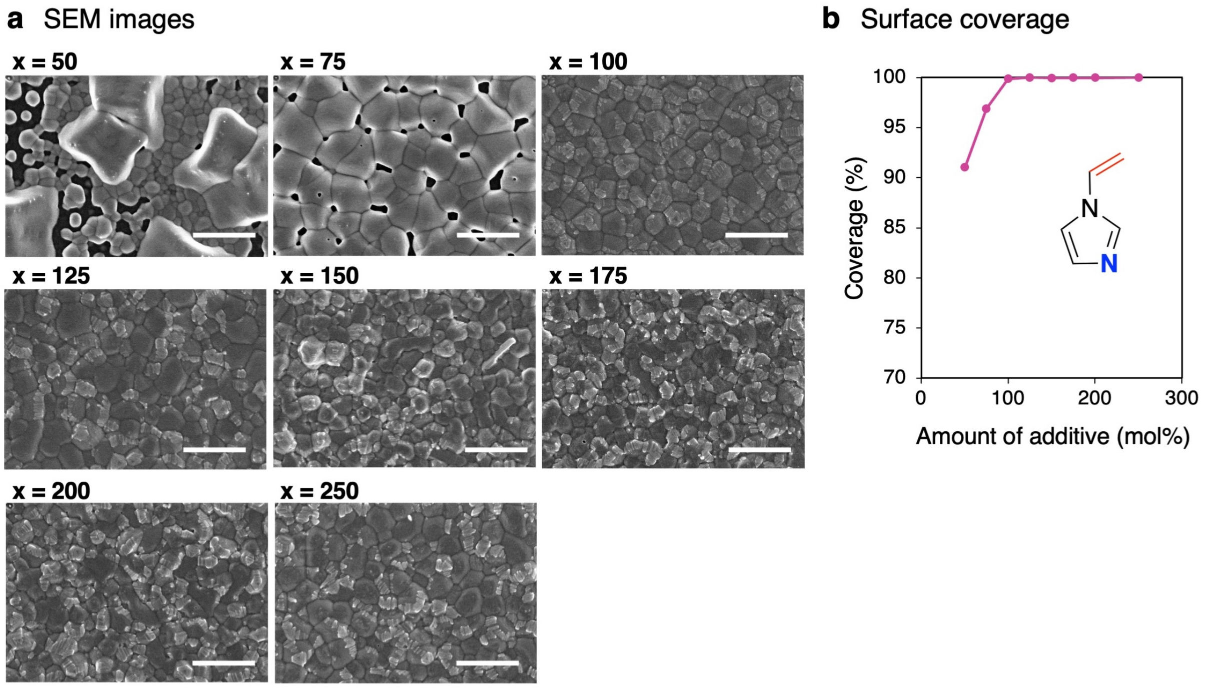

Figure S8. (a) SEM images of tin perovskite thin film fabricated by the vacuum quenching method with different amounts of 1-vinylimidazole. The scale bar represents 1.0 µm. (b) Surface coverage changes with the amount of additive. Coverage was incomplete when 50 mol% and 75 mol% 1-vinylimidazole were added relative to SnI_2. Using more than 100 mol% of 1-vinylimidazole always gave a coverage close to 100%.

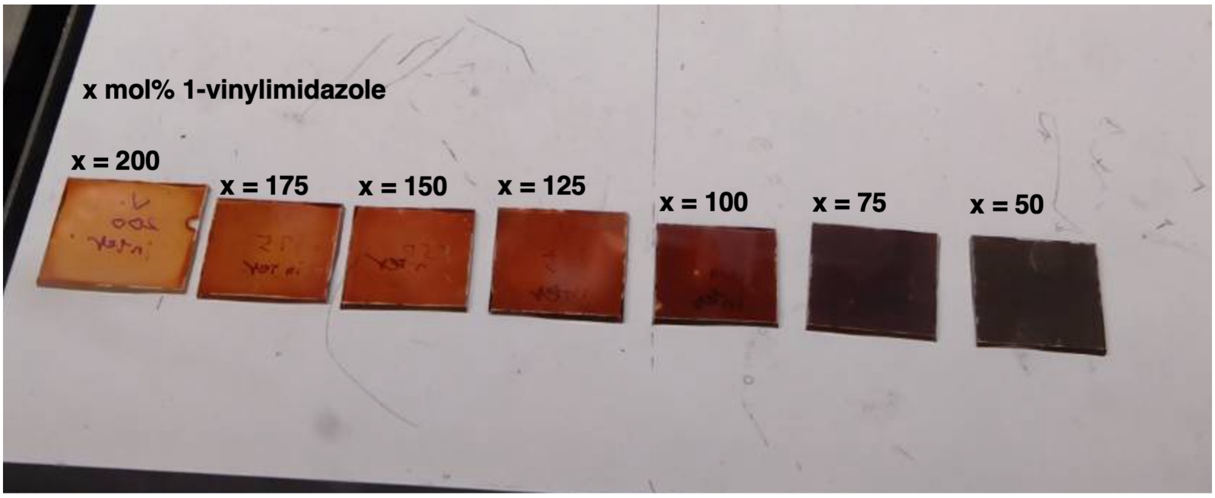

Figure S9. Photographs of the films after vacuum-quenching. Different amounts of vinylimidazole (x mol% relative to SnI_2) were added to the precursor solution.

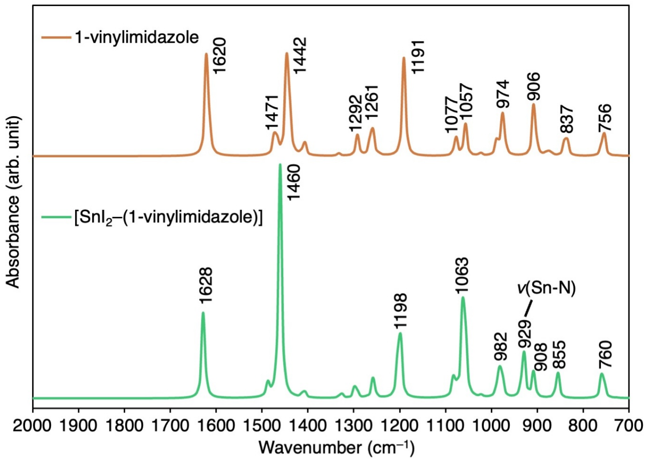

Figure S10. Calculated IR spectra of 1-vinylimidazole and [SnI$_2$–(1-vinylimidazole)] complex. Calculations were done with PW6B95D3/def2-TZVP level of theory (scaling factor = 0.9613).

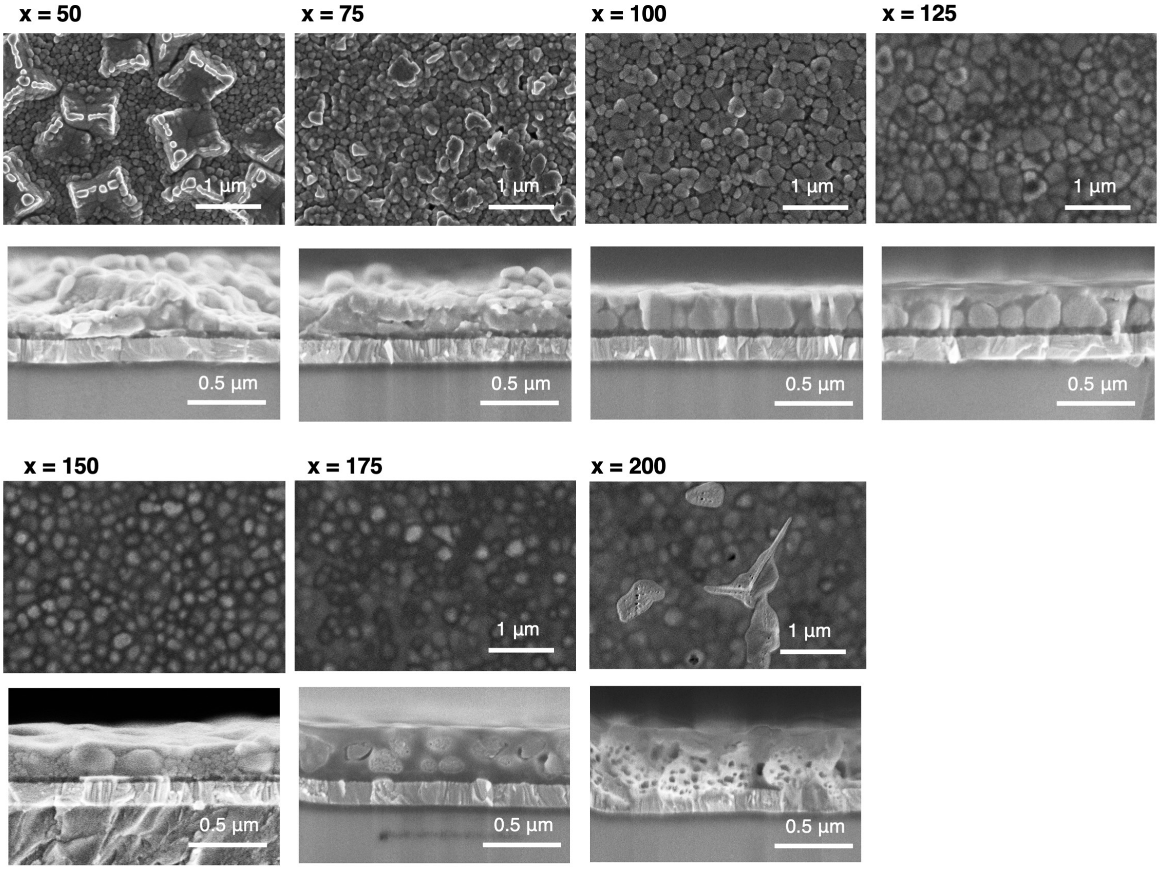

Figure S11. SEM images of intermediate films deposited with different amounts of 1-vinylimidazole additive.

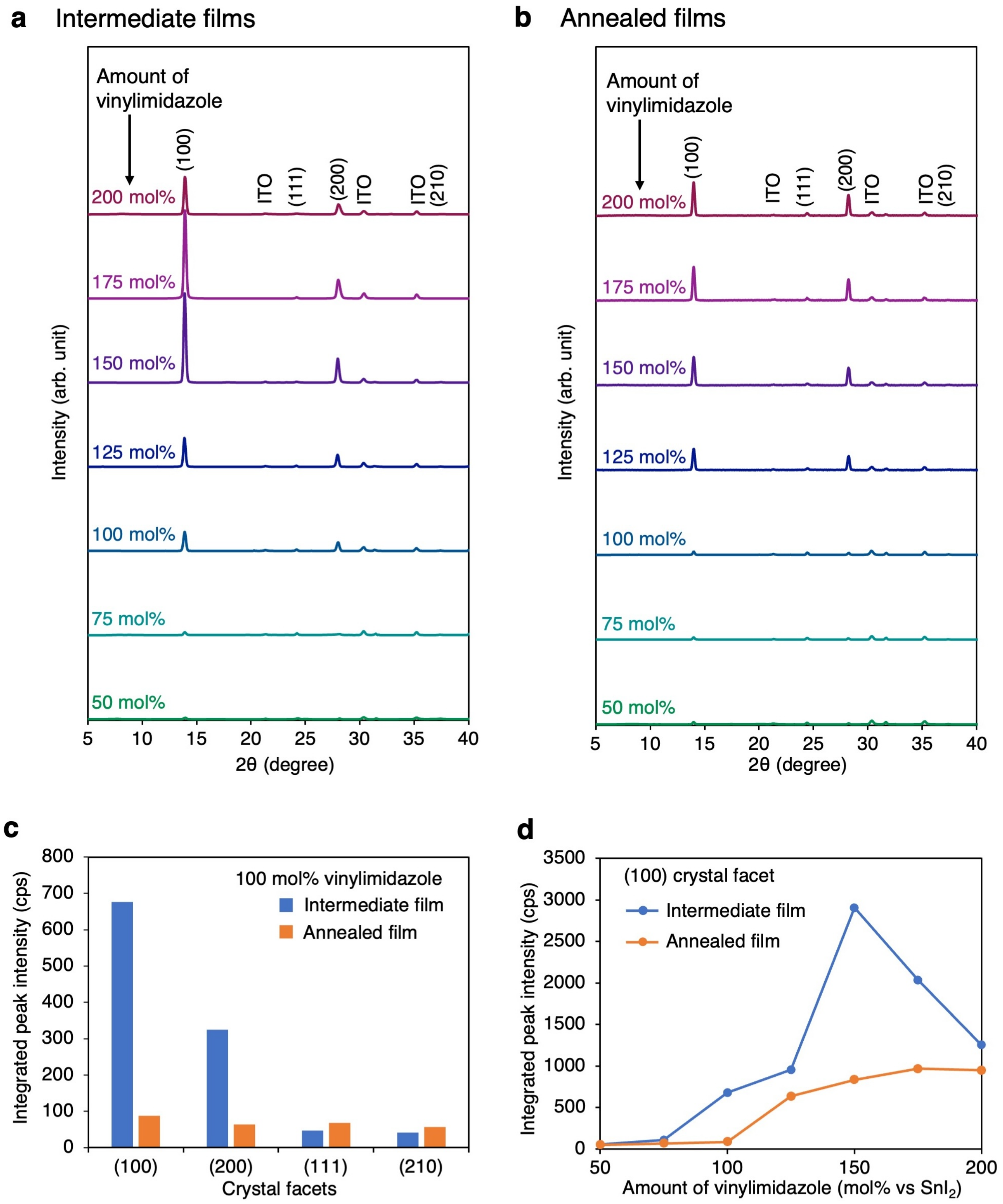

Figure S12. XRD spectrum of (a) intermediate and (b) annealed films fabricated with different amounts of 1-vinylimidazole additive. (c) The changes in the integrated peak intensity of (100), (200), (111), and (210) crystal facets before and after thermal annealing. (d) The changes in the integrated peak intensity of a (100) crystal facet before and after thermal annealing, fabricated with different amounts of 1-vinylimidazole additive.

The perovskite (100) diffraction peaks in the intermediate film are more intense than those of the annealed perovskite film, and (111) and (210) diffractions are very weak. When the amount of 1-vinylimidazole was increased to up to 200 mol%, the diffraction of the (100) crystal facet increased for both the intermediate and the annealed films, suggesting that 1-vinylimidazole likely helps to orient the perovskite crystals.

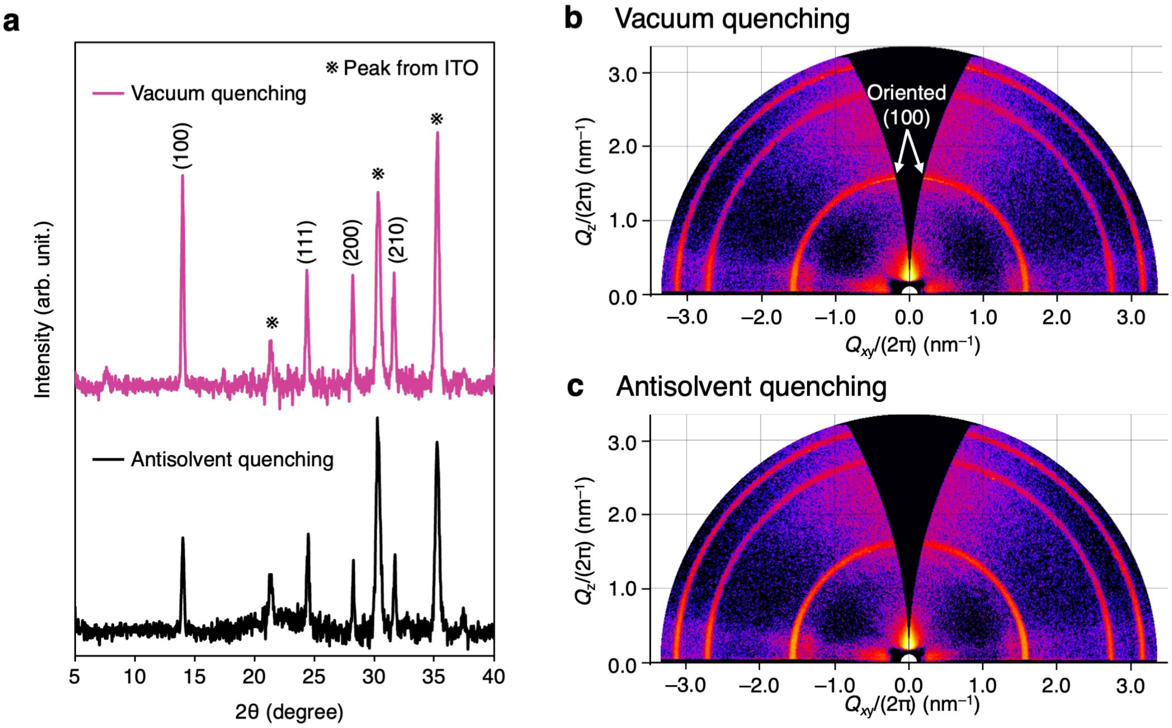

Figure S13. Comparison of the (a) XRD and (b), (c) two-dimensional grazing-incidence X-ray diffraction (2D-GIXD) spectra of tin perovskite thin films fabricated using the vacuum or antisolvent quenching method.

The perovskite film prepared by the V-CGR method had better crystal orientation than comparable films prepared by conventional antisolvent processes.

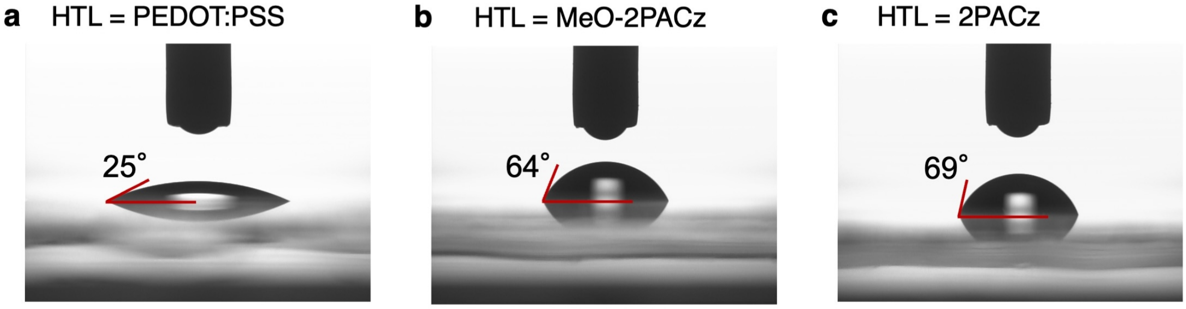

Figure S14. Contact angles of the water droplets on the PEDOT:PSS, MeO-2PACz, and 2PACz on the ITO substrates.

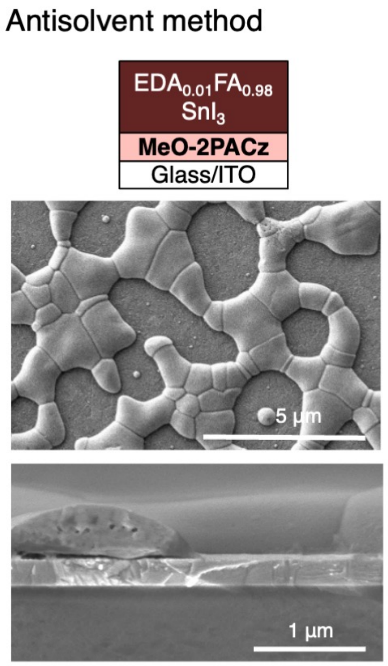

Figure S15. Top and cross-sectional SEM images of $EDA_{0.01}FA_{0.98}SnI_3$ fabricated on MeO-2PACz layer by the antisolvent method.

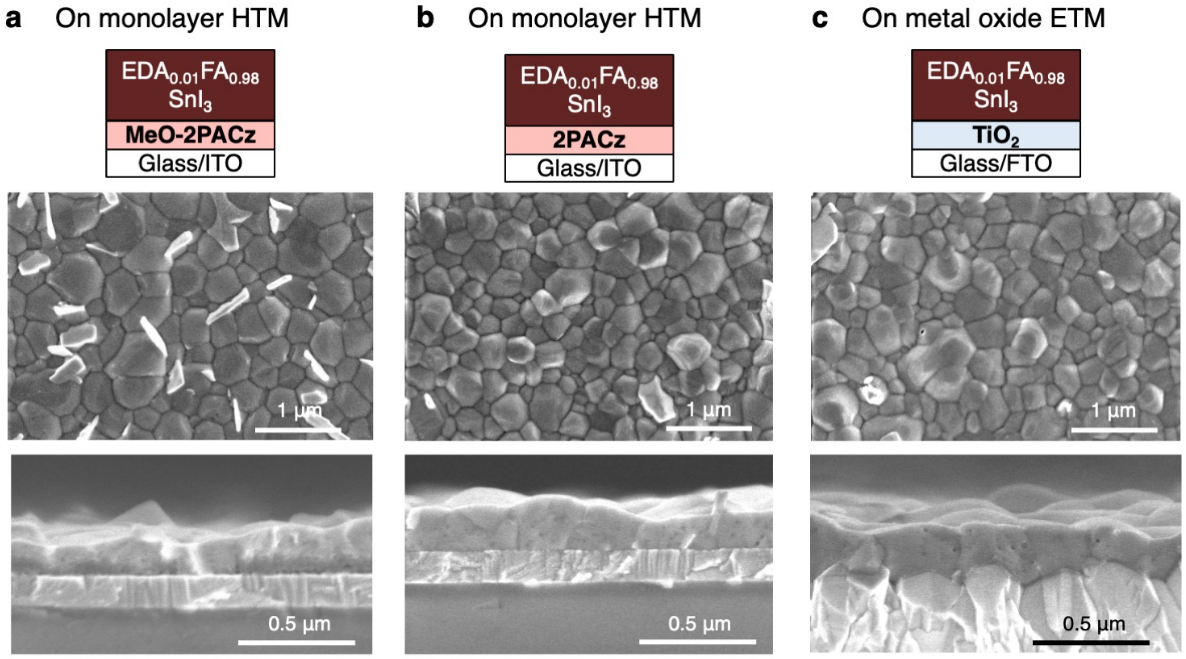

Figure S16. Top and cross-sectional SEM images of $EDA_{0.01}FA_{0.98}SnI_3$ on (a) MeO-2PACz, (b) 2PACz, and (c) TiO_2 underlayers fabricated by the V-CGR method.

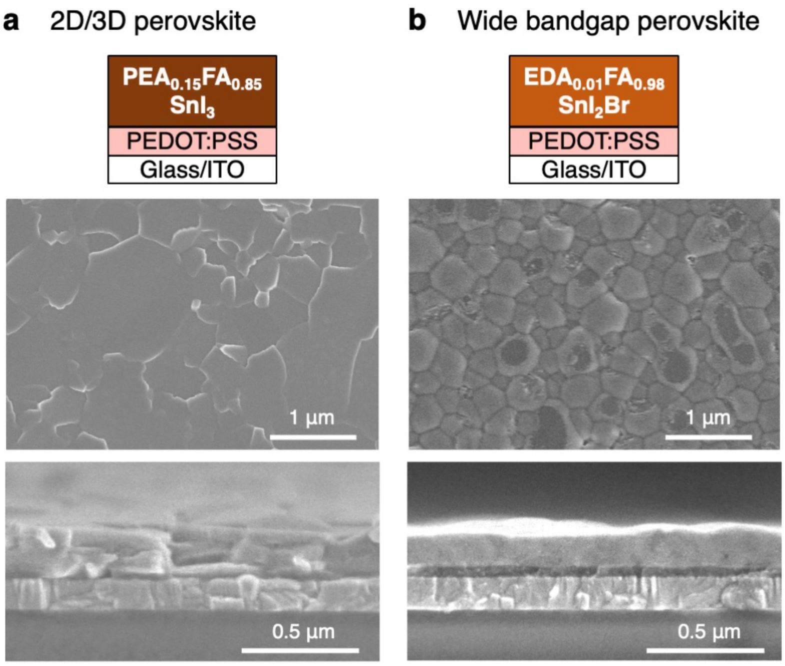

Figure S17. Top and cross-sectional SEM images of 2D/3D $PEA_{0.15}FA_{0.85}SnI_3$, and (d) wide-bandgap $EDA_{0.01}FA_{0.98}SnI_2Br$ fabricated by the V-CGR method.

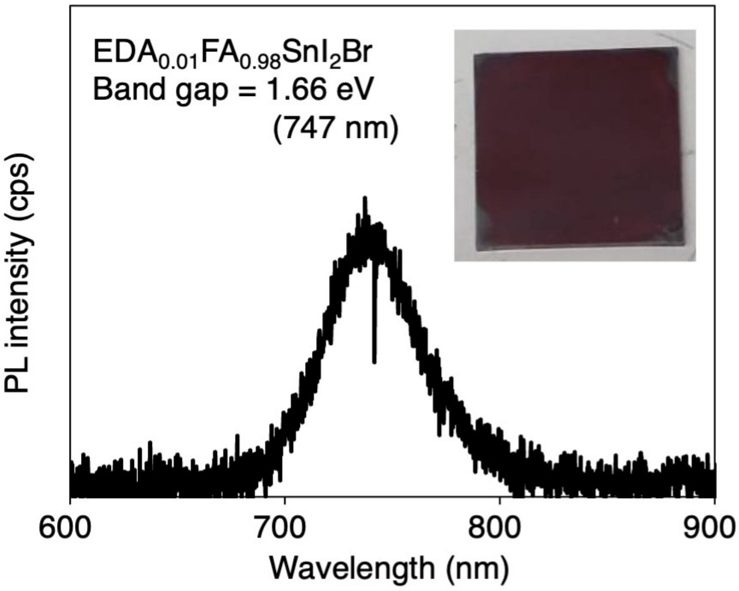

Figure S18. PL spectra and a photograph of $EDA_{0.01}FA_{0.98}SnI_2Br$ perovskite thin film. The optical band gap is estimated to be 1.66 eV (747 nm). This band gap is almost the same as the reported bandgap of $FASnI_2Br$ perovskite (1.68 eV).[12]

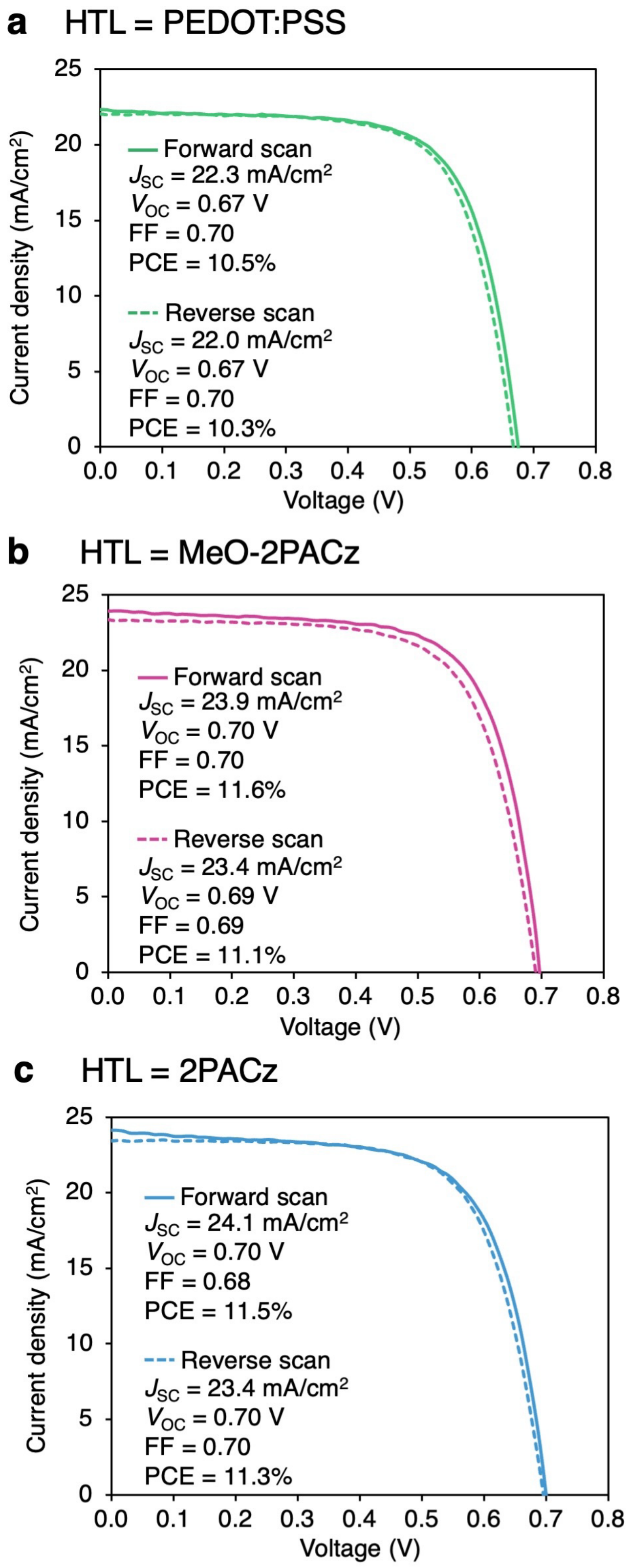

Figure S19. Current density–voltage (*J*–*V*) curves of the solar cells using (a) PEDOT:PSS, (b) MeO-2PACz, and (c) 2PACz as a hole-transporting material.

Table S3. Reports on p-i-n-type tin perovskite solar cells using monolayer-type hole-collecting materials. The reports using ITO/NiO$_x$ substrates were not included.

HTMs	J_{SC} [mA cm^{-2}]	V_{OC} [V]	FF	PCE [%]	Reference
MeO-2PACz	20.3	0.47	0.68	6.5	D. Song, E. W.-G. Diau *et al. ACS Energy Lett.* **2021**, *6*, 4179.[13]
TQxD	21.0	0.57	0.69	8.3	S. F. Afraj, W.-G. Diau *et al. Adv. Funct. Mater.* **2023**, *33*, 2213939.[14]
4-aminobenzoic acid	19.9	0.53	0.72	7.6	A. Abid, W.-G. Diau *et al. Chem. Eng. J.* **2023**, *477*, 146755.[15]
MeO-2PACz	14.3	0.64	0.64	5.8	E. Aktas, A. Abate *et al. ACS Energy Lett.* **2023**, *8*, 5170.[16]
MeO-2PACz	17.6	0.83	0.65	9.4	S. Song, Q. Yu *et al. ACS Energy Lett.* **2024**, *9*, 1466.[17]
TPAT-CA	19.2	0.58	0.73	8.1	S. F. Afraj, W.-G. Diau *et al. Small* **2025**, *21*, 2408638.[18]
Phytic acid dipotassium	18.9	0.91	0.72	12.5	J. Huang, X. Meng *et al. Sci. China Chem.* **2025**, https://doi.org/10.1007/s11426-024-2657-8.[19]
MeO-2PACz	23.9	0.70	0.68	11.6	**This work**

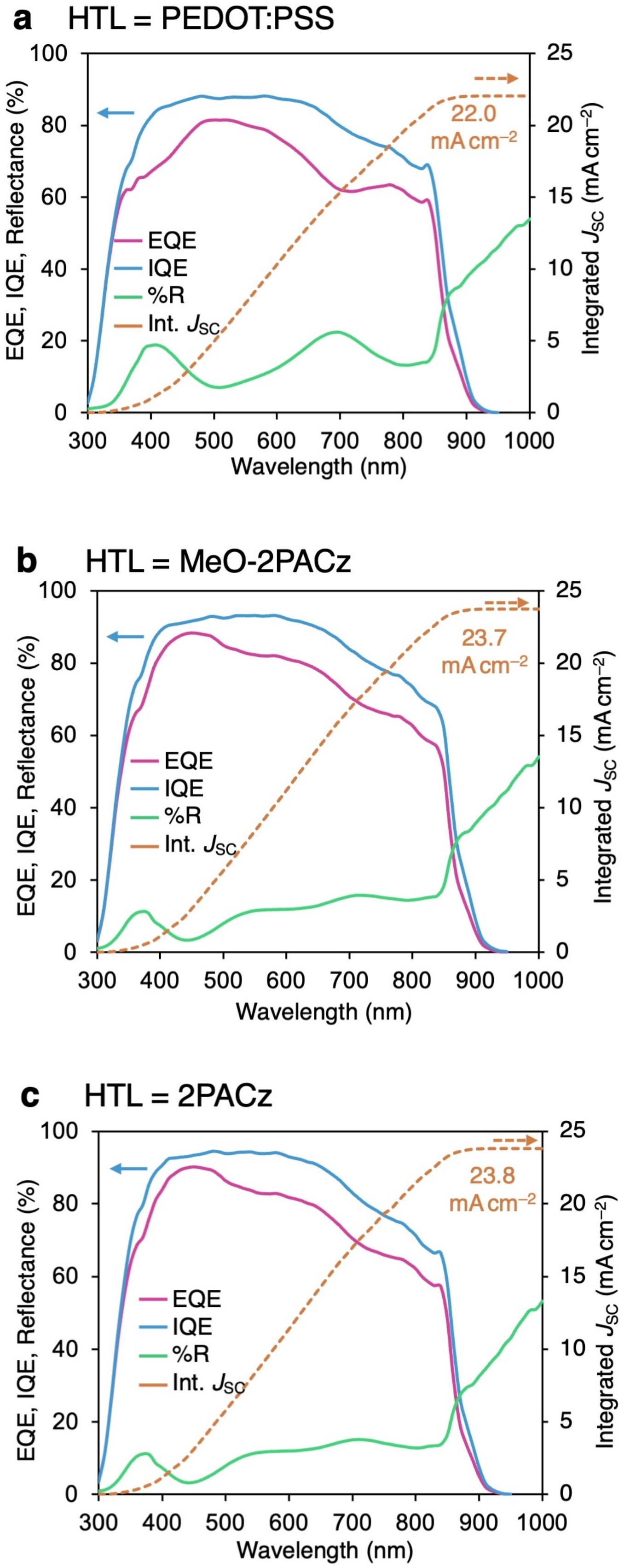

Figure S20. EQE, IQE, reflectance, and integrated J_{SC} of the solar cells using PEDOT:PSS, MeO-2PACz, or 2PACz as a hole-transporting materials.

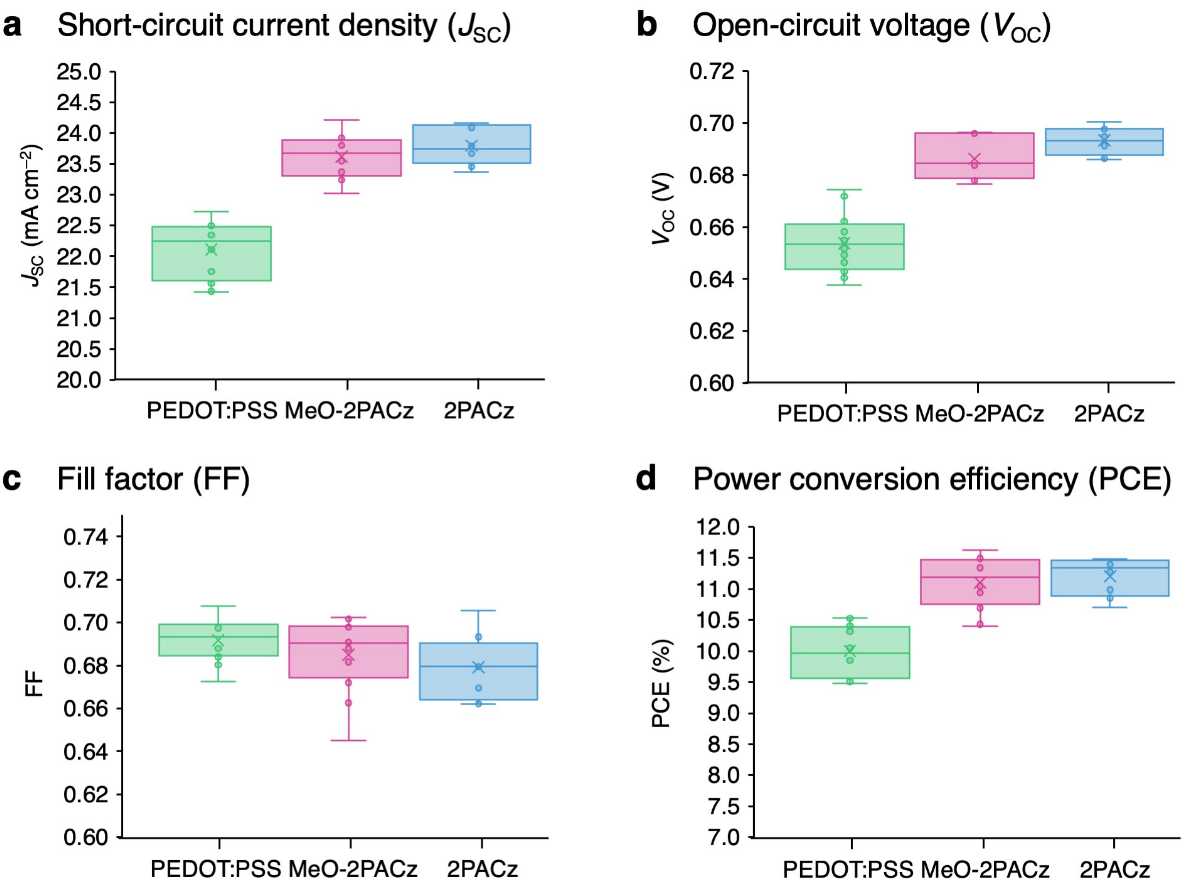

Figure S21. Statistical distribution of photovoltaic parameters of 12 solar cell devices. The individual data points (dots), the range of values (whiskers), the interquartile range with the median value (boxes), the mean value (cross marks) are shown.

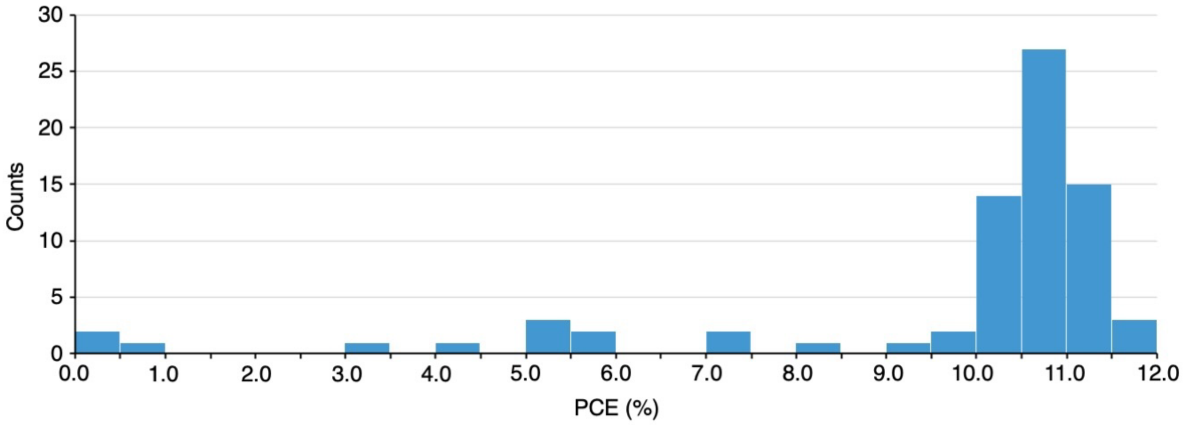

Figure S22. Histogram of the power conversion efficiencies of 75 samples using MeO-2PACz.

Among these, 62 devices achieved a PCE exceeding 9% (process tolerance), corresponding to a yield rate of 82%. The few outliers below this threshold were primarily due to human handling errors rather than process limitations, indicating that the V-CGR method offers a practical level of reproducibility.

Table S4. Photovoltaic parameters of 75 samples. The device structure of ITO/ MeO-2PACz/ EDA$_{0.01}$FA$_{0.98}$SnI$_3$/ EDAI$_2$/ICBA:PCBM /C$_{60}$ /BCP /Ag. A forward scan was used.

No.	J_{SC} [mA cm^{-2}]	V_{OC} [V]	FF	PCE [%]
1	23.4	0.66	0.69	10.7
2	23.5	0.66	0.70	10.9
3	23.4	0.66	0.70	10.9
4	23.6	0.66	0.67	10.5
5	24.9	0.65	0.63	10.1
6	23.9	0.64	0.66	10.2
7	23.9	0.66	0.70	11.0
8	21.4	0.64	0.31	4.2
9	24.2	0.68	0.70	11.6
10	20.6	0.64	0.38	5.1
11	23.9	0.70	0.66	10.9
12	23.4	0.64	0.37	5.5
13	23.8	0.69	0.66	10.8
14	23.8	0.65	0.48	7.5
15	24.1	0.69	0.68	11.5
16	24.1	0.70	0.67	11.2
17	23.6	0.68	0.67	10.8
18	23.1	0.68	0.68	10.8
19	21.9	0.68	0.68	10.1
20	24.5	0.70	0.64	11.0
21	12.7	0.02	0.24	0.0
22	23.7	0.70	0.65	10.9
23	23.1	0.71	0.67	11.0
24	23.1	0.71	0.67	10.9
25	23.7	0.70	0.64	10.6
26	23.7	0.70	0.67	11.3
27	24.2	0.55	0.44	5.9
28	23.5	0.53	0.28	3.5
29	23.8	0.68	0.70	11.3
30	23.5	0.68	0.69	10.9
31	23.4	0.68	0.69	10.9
32	23.0	0.68	0.66	10.4
33	23.2	0.68	0.67	10.7
34	23.3	0.70	0.68	11.0
35	23.7	0.40	0.56	5.3
36	23.9	0.68	0.70	11.4
37	23.5	0.68	0.65	10.4
38	23.9	0.70	0.70	11.6
39	23.9	0.70	0.69	11.5
40	23.8	0.70	0.69	11.4
41	24.0	0.66	0.67	10.6
42	23.8	0.65	0.65	10.0
43	23.6	0.64	0.66	9.9
44	24.4	0.66	0.66	10.6
45	24.3	0.66	0.69	10.9
46	23.0	0.69	0.70	11.1
47	22.9	0.69	0.71	11.2
48	22.9	0.67	0.65	9.9
49	22.8	0.69	0.69	10.8
50	23.0	0.69	0.70	11.1
51	23.0	0.69	0.69	10.9
52	0.0	0.00	0.00	0.0
53	23.0	0.69	0.63	10.0
54	20.7	0.18	0.25	0.9
55	17.5	0.66	0.64	7.5
56	13.8	0.60	0.64	5.3
57	19.2	0.66	0.65	8.3
58	24.4	0.63	0.66	10.1
59	24.4	0.62	0.68	10.2
60	24.1	0.63	0.69	10.5
61	24.3	0.66	0.72	11.6
62	24.1	0.65	0.72	11.4
63	23.9	0.65	0.72	11.2
64	24.1	0.64	0.70	10.9

No.	J_{SC} [mA cm^{-2}]	V_{OC} [V]	FF	PCE [%]
65	24.1	0.64	0.72	11.2
66	24.1	0.64	0.72	11.0
67	22.5	0.67	0.68	10.4
68	22.4	0.67	0.70	10.5
69	22.8	0.67	0.71	10.7
70	22.9	0.67	0.69	10.5

No.	J_{SC} [mA cm^{-2}]	V_{OC} [V]	FF	PCE [%]
71	22.9	0.67	0.70	10.7
72	22.7	0.66	0.62	9.2
73	22.4	0.66	0.68	10.1
74	22.5	0.67	0.71	10.7
75	22.5	0.67	0.71	10.8

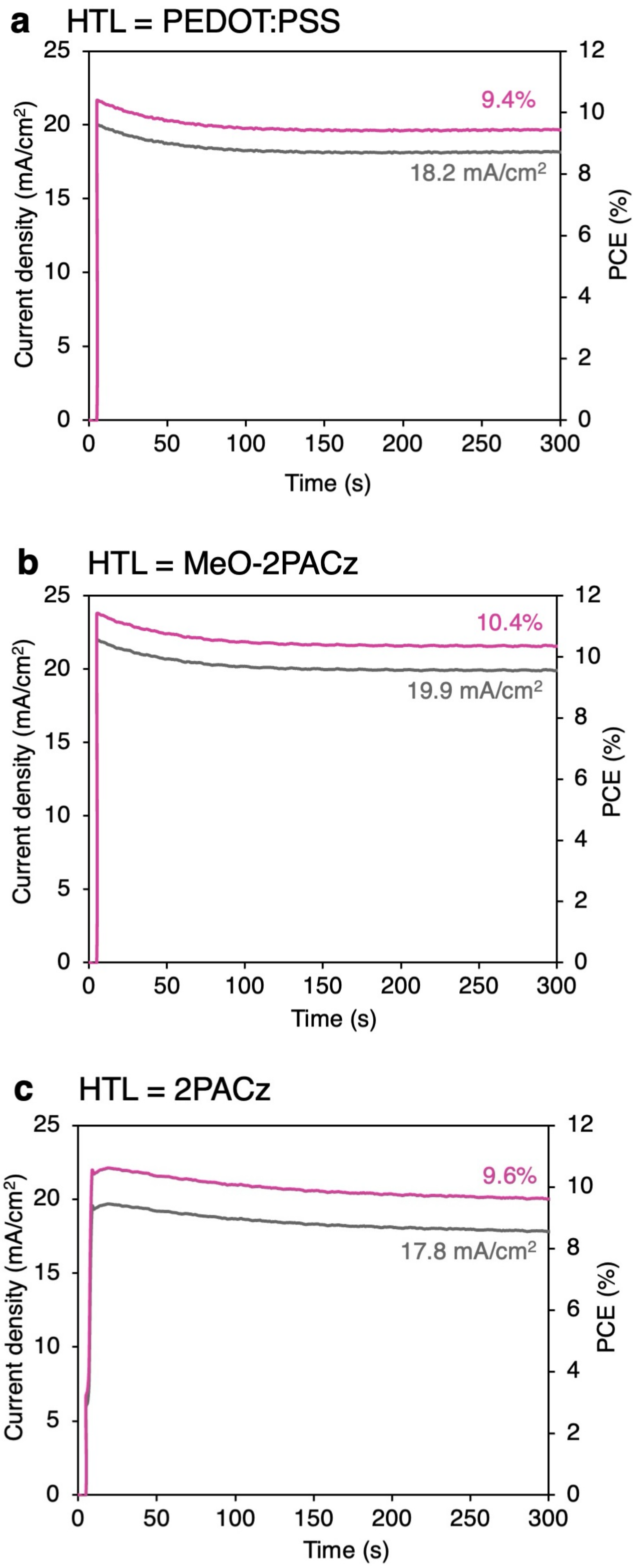

Figure S23. Stabilized current density (black line) and stabilized power output (red line) of representative tin perovskite solar cells using (a) PEDOT:PSS, (b) MeO-2PACz, and (c) 2PACz as HTM. The measurements were performed under AM 1.5G, 100 mW cm^{-2} irradiation at a bias of 0.44 V for the device using PEDOT:PSS, 0.51 V for the device using MeO-2PACz, and 0.54 V for the device using 2PACz.

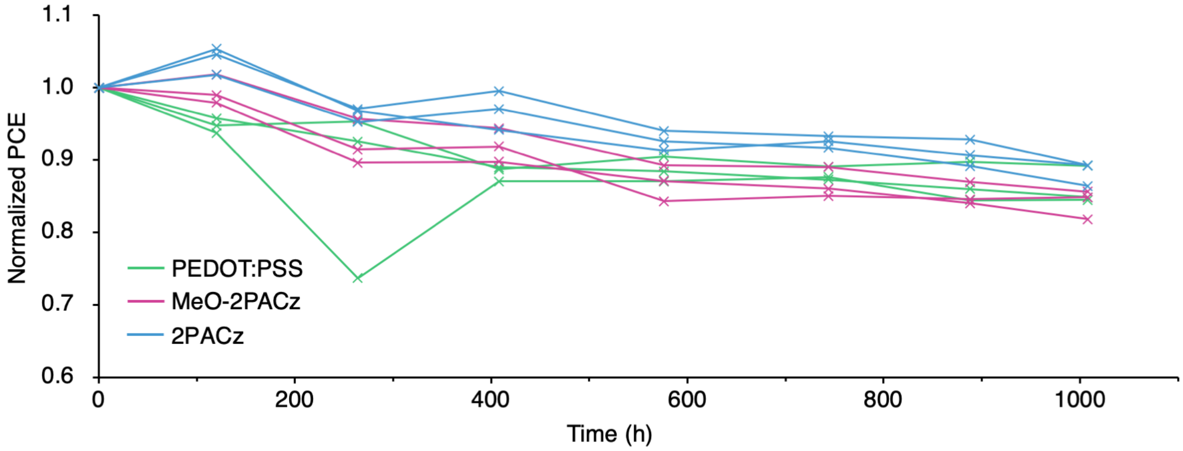

Figure S24. Shelf-stability of Sn PSCs in a nitrogen-filled glovebox, room temperature, and dark conditions. Individual data are shown.

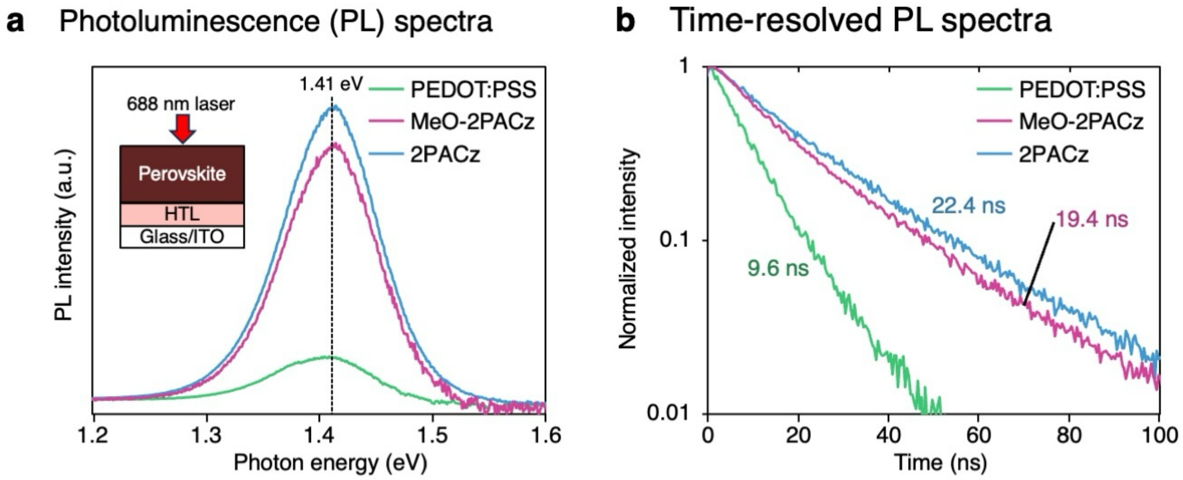

Figure S25. (a) Photoluminescence (PL) and (b) time-resolved PL spectra of tin perovskite films prepared on PEDOT:PSS, MeO-2PACz, and 2PACz.

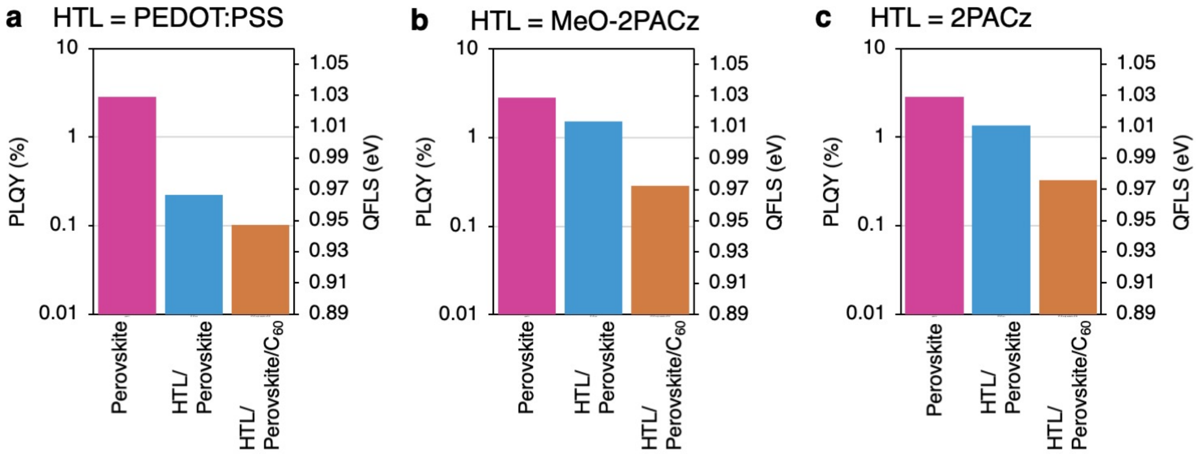

Figure S26. Photoluminescence quantum yield (PLQY) for perovskite films on the quartz substrates, hole-transporting layer (HTL)/perovskite stack, and HTL/perovskite/C_{60}. For HTL/perovskite/C_{60} samples, perovskite films were passivated by a 1 nm-thick $EDAI_2$ and 1 mg/mL PCBM/ICBA mixed solution. (a) PEDOT:PSS, (b) MeO-2PACz, and (c) 2PACz were used as an HTL.

The PLQY of the perovskite film deposited on quartz substrates was 2.82%, corresponding to an estimated quasi-Fermi level splitting (QFLS) of 1.03 eV. When perovskite films were deposited on PEDOT:PSS, the PLQY decreased to 0.22% (QFLS = 0.97 eV), indicating severe interfacial non-radiative recombination. In contrast, perovskite films deposited on monolayer HTMs (MeO-2PACz and 2PACz) retained much higher PLQY values of 1.52% and 1.36%, respectively (QFLS = 1.01 eV). From these results, we can conclude that non-radiative recombination was suppressed by using monolayer-type HTMs, accounting for the higher V_{OC} obtained in the solar cells. However, when C_{60} layers were stacked on the monolayer HTL/perovskite films, the PLQY dropped by nearly one order of magnitude (QFLS = 0.97 eV). This strong quenching indicates pronounced interfacial recombination, which we estimate to introduce a V_{OC} loss of at least 0.04 V.

Note that a substantial gap still remains between the QFLS and the device V_{OC}. The remaining V_{OC} loss (~0.3 eV) can be attributed to the large energy offset between the LUMO of C_{60} (–4.2 eV) and the CBM of the perovskite (–3.6 eV).

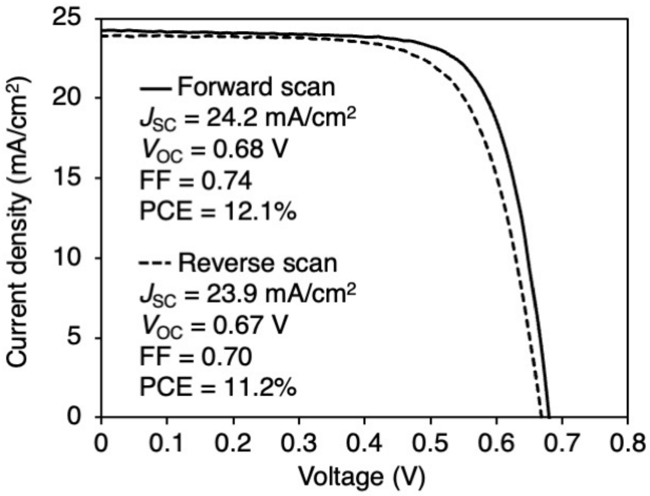

Figure S27. Current-voltage (*J–V*) curves of the campion cells. Three modifications were made to the standard fabrication procedure. First, 1 mol% NH_4SCN (relative to SnI_2) was added to the perovskite precursor solution as an additive.[20] Second, 2 mg mL^{-1} Al_2O_3 solution in IPA was spin-coated on the MeO-2PACz layer (slope 5 s / 3,000 rpm, 30 s / slope 1 s).[21] Third, the concentration of PCBM/ICBA mixed solution for surface treatment was increased from 1 mg mL^{-1} to 4 mg mL^{-1}. Al_2O_3 nanopowder (13 nm primary particle size, 99.8% trace metal basis) was purchased from Sigma-Aldrich Co., Ltd. To prepare the Al_2O_3 solution, Al_2O_3 powder (3.0 g) was dispersed in IPA (30 mL) and was ultrasonicated for over 1 day. The resulting dispersion was centrifuged (10,000 rpm, 15 min), and the supernatant was collected. This process was repeated twice. Finally, the supernatant was diluted to 2 mg mL^{-1} and filtered through a 0.20 μm PTFE filter.

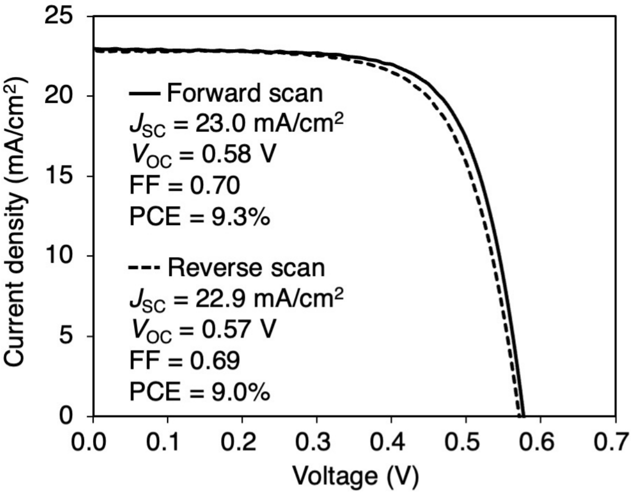

Figure S28. Current-voltage (*J*–*V*) curves of the campion cells fabricated by an antisolvent method using DMSO an a solvent.

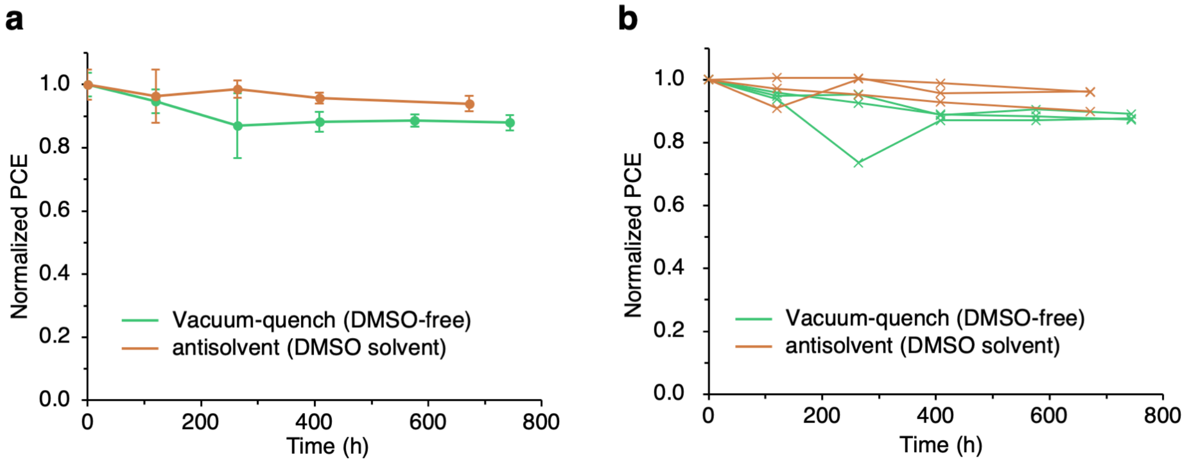

Figure S29. Shelf-stability of Sn PSCs in an N_2-filled glovebox, room temperature, and dark conditions. Three individual samples were used per condition. (a) Average values (dots) and the standard deviation (whiskers) are shown. (b) Individual data are shown.

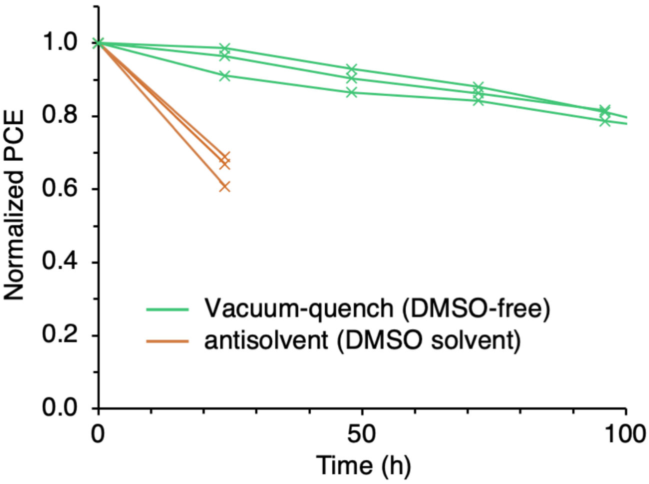

Figure S30. Thermal stability of Sn PSCs at 85 °C. Individual data are shown.

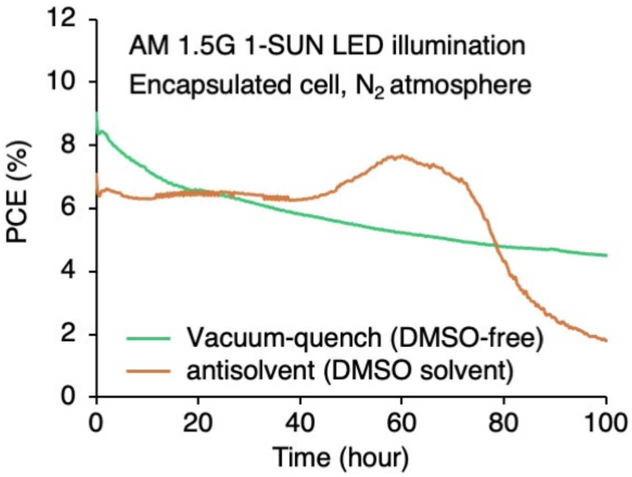

Figure S31. Maximum power point tracking (MPPT) under 1 sun continuous light illumination (100 mW cm^{-2}, ISOS-L1) on the encapsulated Sn PSCs in a nitrogen atmosphere.

For the device fabricated by the V-CGR method on PEDOT:PSS, the PCE decreased from 9.0% to 4.5% after 100 h of continuous operation, accompanied by a reduction in all photovoltaic parameters (J_{SC}, V_{OC}, and FF). A comparable efficiency drop was also observed for the device prepared by the conventional antisolvent method.

Thermal stability tests indicate that degradation in the dark is largely attributed to Sn(II) oxidation caused by residual DMSO (Figure 4e). However, the finding that the devices prepared by DMSO-free V-CGR method also degrade under illumination suggests that a different degradation mechanism dominates during illumination.

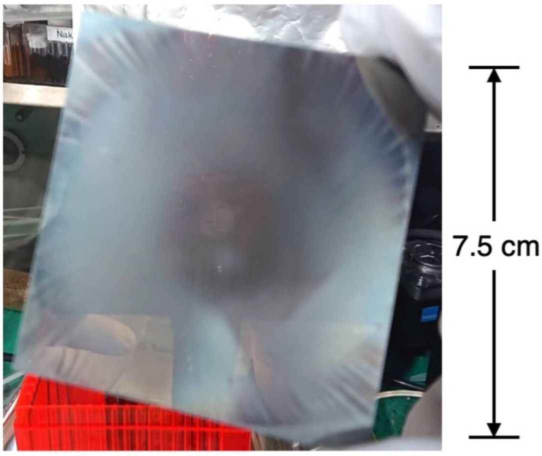

Figure S32. The picture of tin perovskite thin film fabricated on a 7.5 by 7.5 cm^2 substrate by antisolvent method.

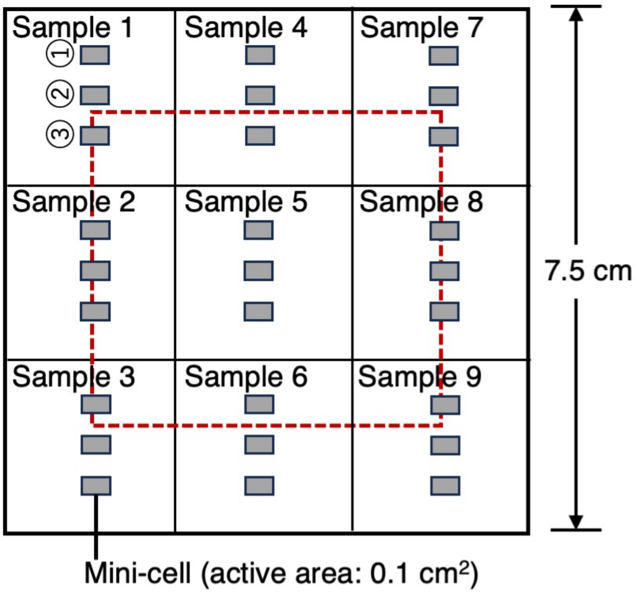

Figure S33. The layout of mini-cells on the 7.5 by 7.5 cm^2 perovskite film. 7.5 by 7.5 cm^2 substrate was cut into nine 2.5 by 2.5 cm^2 pieces. Each small substrate has 3 mini-cells with an active area of 0.14 cm^2. The red dashed line represents the approximate active area of the solar module fabricated in this work.

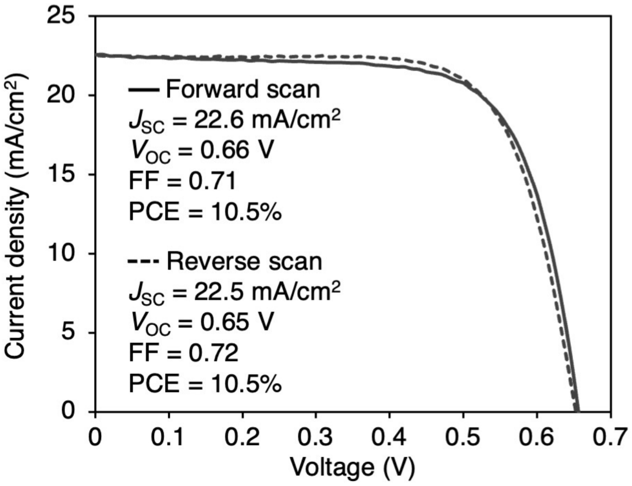

Figure S34. Current-voltage (*J*–*V*) curves of the campion cells using the 7.5 by 7.5 cm^2 perovskite film fabricated on PEDOT:PSS hole-transporting material.

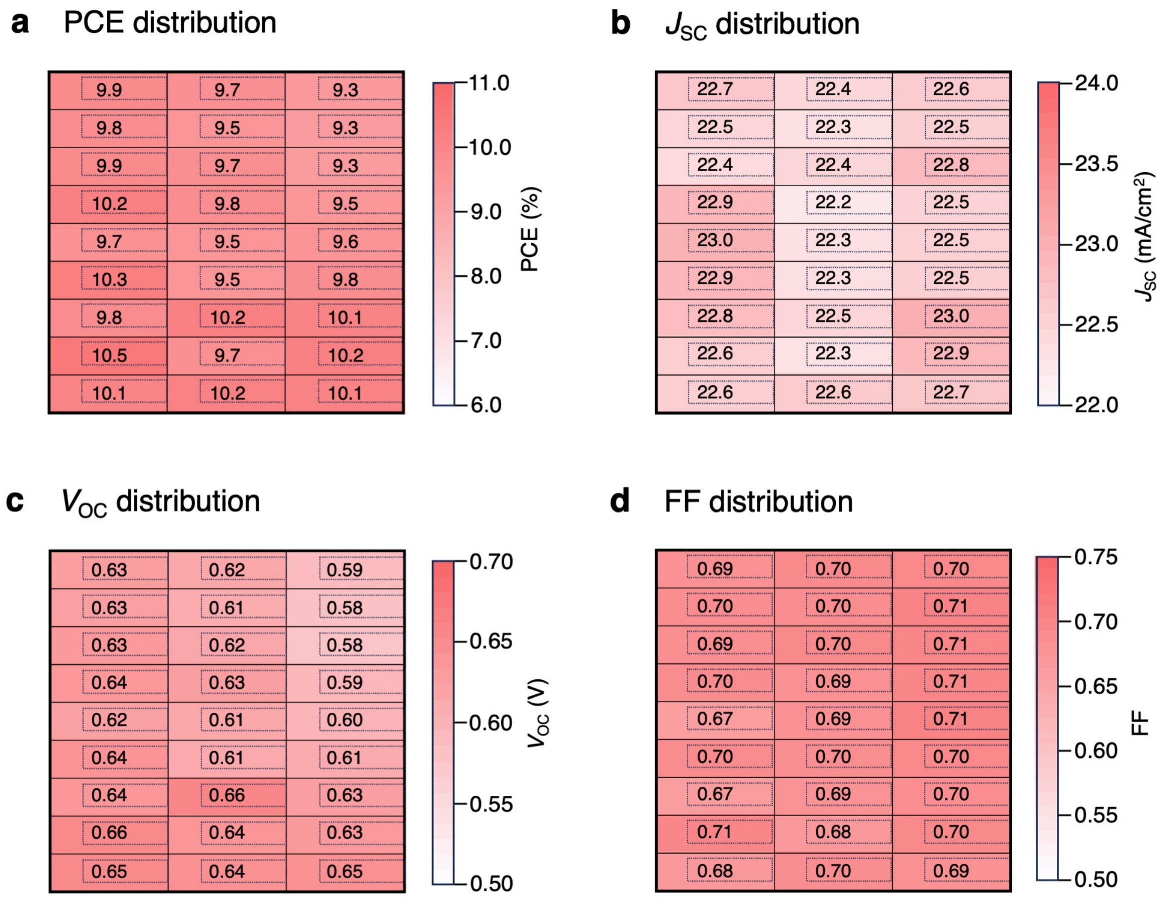

PCE distribution

9.9	9.7	9.3
9.8	9.5	9.3
9.9	9.7	9.3
10.2	9.8	9.5
9.7	9.5	9.6
10.3	9.5	9.8
9.8	10.2	10.1
10.5	9.7	10.2
10.1	10.2	10.1

J_{SC} distribution

22.7	22.4	22.6
22.5	22.3	22.5
22.4	22.4	22.8
22.9	22.2	22.5
23.0	22.3	22.5
22.9	22.3	22.5
22.8	22.5	23.0
22.6	22.3	22.9
22.6	22.6	22.7

V_{OC} distribution

0.63	0.62	0.59
0.63	0.61	0.58
0.63	0.62	0.58
0.64	0.63	0.59
0.62	0.61	0.60
0.64	0.61	0.61
0.64	0.66	0.63
0.66	0.64	0.63
0.65	0.64	0.65

FF distribution

0.69	0.70	0.70
0.70	0.70	0.71
0.69	0.70	0.71
0.70	0.69	0.71
0.67	0.69	0.71
0.70	0.70	0.70
0.67	0.69	0.70
0.71	0.68	0.70
0.68	0.70	0.69

Figure S35. Distributions of photovoltaic parameters of 27 mini-cells using the 7.5 by 7.5 cm^2 perovskite film fabricated on PEDOT:PSS hole-transporting layer.

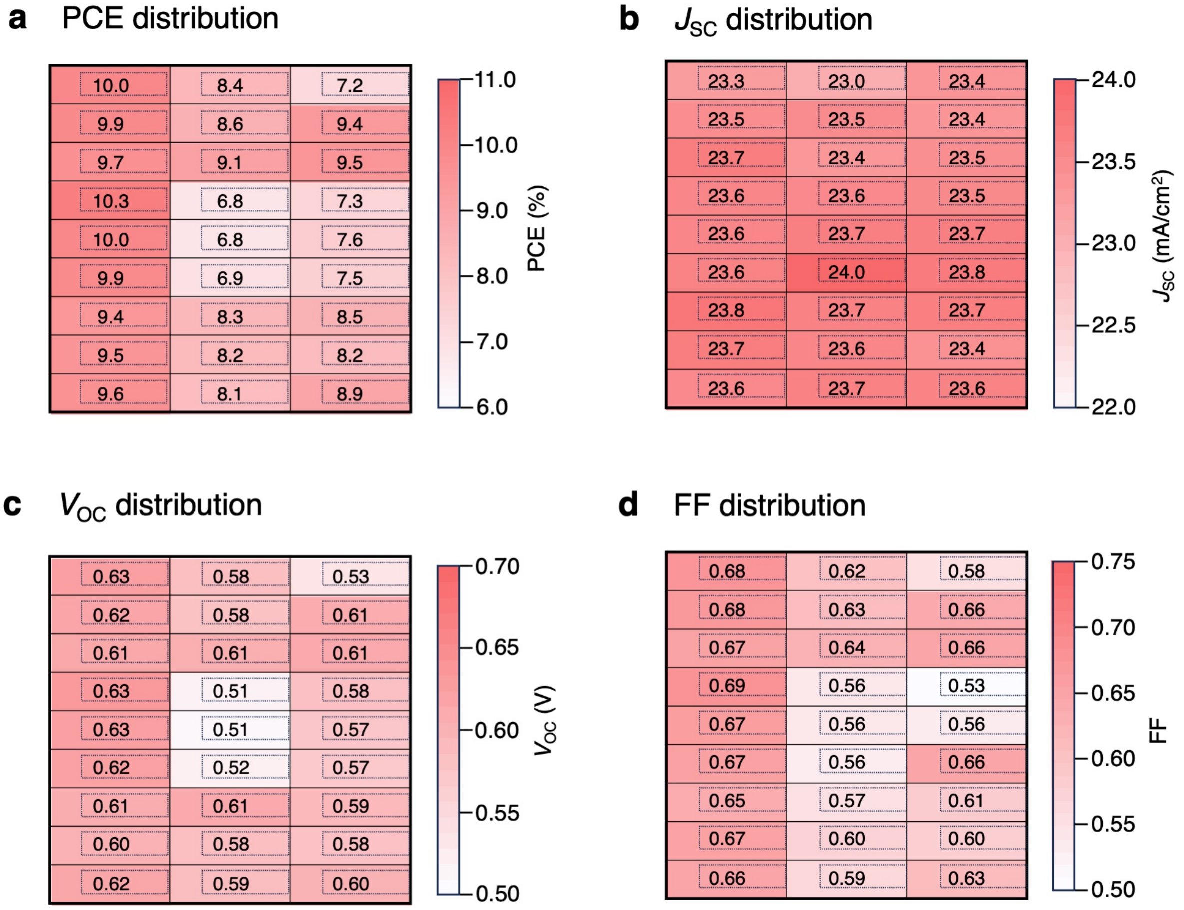

a PCE distribution

10.0	8.4	7.2
9.9	8.6	9.4
9.7	9.1	9.5
10.3	6.8	7.3
10.0	6.8	7.6
9.9	6.9	7.5
9.4	8.3	8.5
9.5	8.2	8.2
9.6	8.1	8.9

b J_{SC} distribution

23.3	23.0	23.4
23.5	23.5	23.4
23.7	23.4	23.5
23.6	23.6	23.5
23.6	23.7	23.7
23.6	24.0	23.8
23.8	23.7	23.7
23.7	23.6	23.4
23.6	23.7	23.6

c V_{OC} distribution

0.63	0.58	0.53
0.62	0.58	0.61
0.61	0.61	0.61
0.63	0.51	0.58
0.63	0.51	0.57
0.62	0.52	0.57
0.61	0.61	0.59
0.60	0.58	0.58
0.62	0.59	0.60

d FF distribution

0.68	0.62	0.58
0.68	0.63	0.66
0.67	0.64	0.66
0.69	0.56	0.53
0.67	0.56	0.56
0.67	0.56	0.66
0.65	0.57	0.61
0.67	0.60	0.60
0.66	0.59	0.63

Figure S36. Distributions of photovoltaic parameters of 27 mini-cells using the 7.5 by 7.5 cm^2 perovskite film fabricated on MeO-2PACz hole-transporting layer.

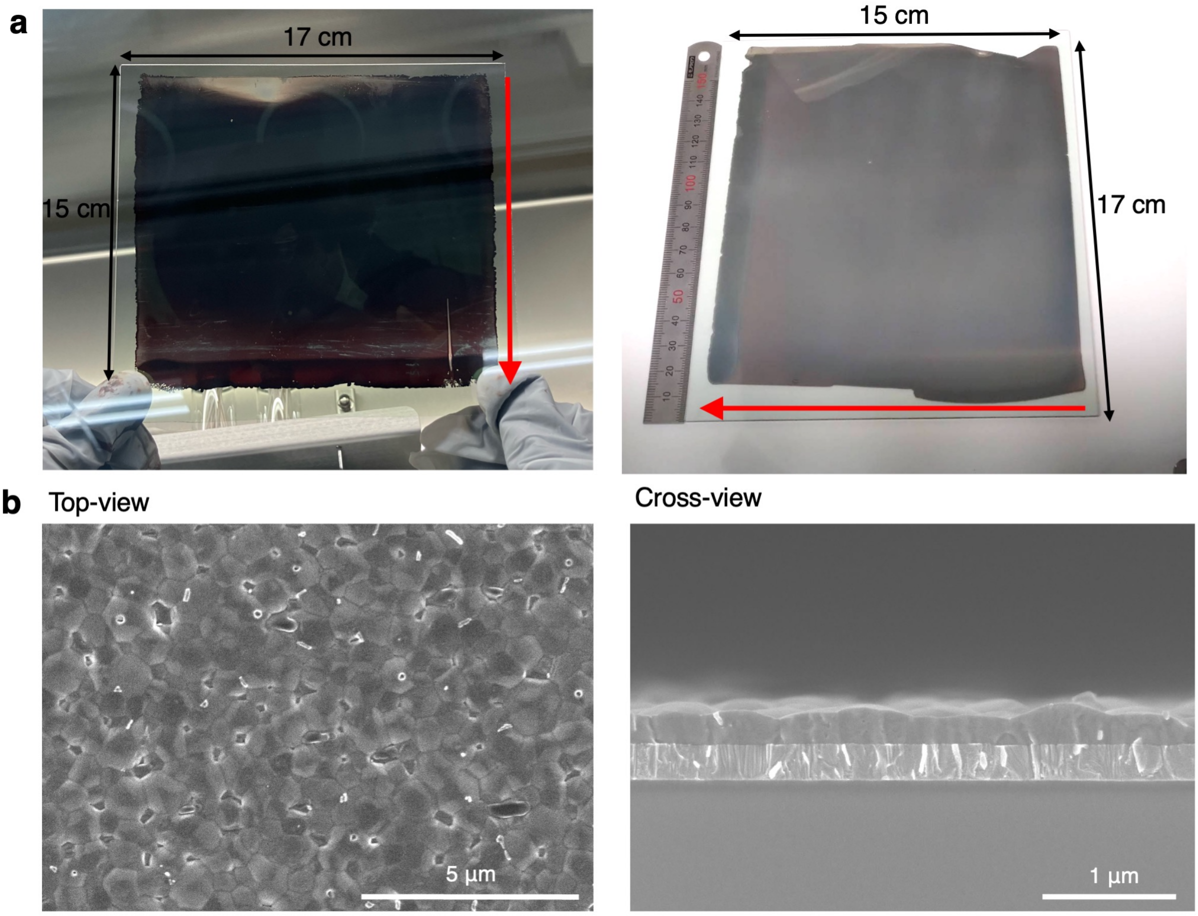

Figure S37. (a) The picture of tin perovskite thin film fabricated on a 17 by 15 cm^2 substrate by slot die coating. The red arrow indicates the direction of slot die coating. (b) Top- and cross-view SEM images of the tin perovskite thin film fabricated by die-coating.

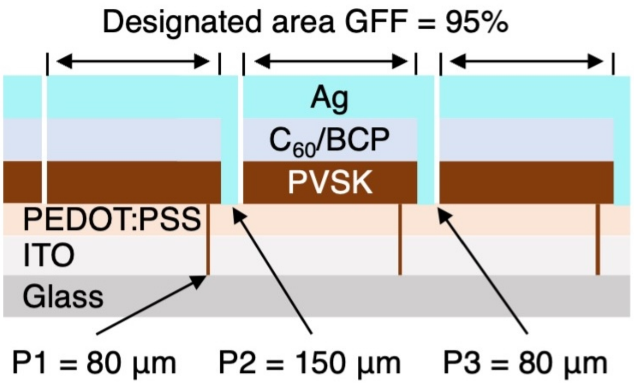

Figure S38. Design of tin perovskite solar modules with an active area of 21.6 cm^2.

Compared to the small-area cell (V_{OC} = 0.67 V, FF =0.70, PCE = 10.4%), the 7-cell module showed a moderate efficiency drop (V_{OC} = 0.59 V/cell, FF =0.60, PCE = 6.8 %). The origins of the V_{OC} and FF losses are discussed below.

In the film uniformity test by fabricating 27 mini-cells (active area: 0.1 cm^2) on a 7.5 by 7.5 cm^2 substrate, all devices showed nearly identical J_{SC} and FF values, while a slight variation was observed in V_{OC} (0.58–0.65 V, Figure S35). This distribution likely contributed to the reduced module V_{OC}. We ascribe this V_{OC} variation to the spatial differences in drying rate and airflow during pressure reduction, leading to local variations in perovskite crystallization and film morphology. Further optimization of the vacuum-drying chamber design and the drying process conditions would minimize this variation.

Regarding the FF drop, the series resistance (R_s) of the 7-cell module (7 Ω cm^2) is approximately twice that of the small cell (3.5 Ω cm^2). Given the uniform distribution of FF of the 27 mini-cells, we conclude that the increase in series resistance mainly originates from the scribing process. Specifically, incomplete removal of the perovskite layer during the P2 scribing step likely introduces additional contact resistance at the Ag electrode/ITO interface.

Table S5. Photovoltaic parameters of the champion tin perovskite solar module.

Scan	I_{SC} [mA]	J_{SC} [mA cm^{-2}]	V_{OC} [V]	FF	PCE [%]
Forward	59.2	19.1	4.17	0.60	6.83
Reverse	58.1	18.8	4.15	0.60	6.71

Table S6. Reports on tin perovskite solar cells and modules with an active area of larger than 1 cm^2.

Active area [cm^2]	Device type	J_{SC} [mA cm^{-2}]	V_{OC} [V]	FF	PCE [%]	Reference
1.02	cell	19.59	0.53	0.61	6.3	T. H. Chowdhury, A. Islam *et al. Sol. RRL* **2019**, *3*, 1900245.[22]
1	cell	17.57	0.56	0.72	7.1	C. Ran, Z. Wu *et al, Joule* **2019**, *3*, 3072. [23]
1	cell	20.25	0.63	0.61	7.8	T. Ye, S. Priya *et al. ACS Energy Lett.* **2021**, *6*, 1480. [24]
1.02	cell	19.96	0.77	0.66	10.1	X. Liu, L. Han *et al. ACS Energy Lett.* **2022**, *7*, 425.[25]
1.02	cell	22.69	0.78	0.69	12.05	B. Li, Z. Zhu *et al. Adv. Mater.* **2023**, 2309768. [26]
1	cell	19.8	0.68	0.66	8.9	Z. Zhang, A. Abate *et al. Adv. Funct. Mater.* **2024**, *34*, 2306458. [27]
1	cell	21.6	0.59	0.66	8.35	W. Żuraw, Ł. Przypis *et al. ACS Energy Lett.* **2024**, *9*, 4509. [28]
12	**module**	16.04	4.85	0.59[a)]	5.7	W. Żuraw, S. Öz *et al. ACS Energy Lett.* **2023**, *8*, 4885. [29]
21.6	**module**	19.1	4.17	0.60	6.8	**This work**

[a)] FF was calculated by the authors, as the value is not provided in the paper.

References

1. Al-Ashouri, A.; Magomedov, A.; Roß, M.; Jošt, M.; Talaikis, M.; Chistiakova, G.; Bertram, T.; Márquez, J. A.; Köhnen, E.; Kasparavičius, E.; Levcenco, S.; Gil-Escrig, L.; Hages, C. J.; Schlatmann, R.; Rech, B.; Malinauskas, T.; Unold, T.; Kaufmann, C. A.; Korte, L.; Niaura, G.; Getautis, V.; Albrecht, S. Conformal monolayer contacts with lossless interfaces for perovskite single junction and monolithic tandem solar cells. *Energy Environ. Sci.* **2019**, *12*, 3356–3369.
2. Hu, S.; Pascual, J.; Liu, W.; Funasaki, T.; Truong, M. A.; Hira, S.; Hashimoto, R.; Morishita, T.; Nakano, K.; Tajima, K.; Murdey, R.; Nakamura, T.; Wakamiya, A. A Universal Surface Treatment for p–i–n Perovskite Solar Cells. *ACS Appl. Mater. Interfaces* **2022**, *14*, 56290–56297.
3. Wang, L.; Miao, Q.; Wang, D.; Chen, M.; Bi, H.; Liu, J.; Baranwal, A. K.; Kapil, G.; Sanehira, Y.; Kitamura, T.; Ma, T.; Zhang, Z.; Shen, Q.; Hayase, S. 14.31 % Power Conversion Efficiency of Sn-Based Perovskite Solar Cells via Efficient Reduction of Sn^{4+}. *Angew. Chem., Int. Ed.* **2023**, *62*, e202307228.
4. Sheldrick, G. M. Crystal Structure Refinement with SHELXL. *Acta Crystallogr C Struct. Chem.* **2015**, *71*, 3.
5. Stolterfoht, M.; Caprioglio, P.; Wolff, C. M.; Márquez, J. A.; Nordmann, J.; Zhang, S.; Rothhardt, D.; Hörmann, U.; Amir, Y.; Redinger, A.; Kegelmann, L.; Zu, F.; Albrecht, S.; Koch, N.; Kirchartz, T.; Saliba, M.; Unold, T.; Neher, D. The Impact of Energy Alignment and Interfacial Recombination on the Internal and External Open-Circuit Voltage of Perovskite Solar Cells. *Energy Environ. Sci.* **2019**, *12*, 2778.
6. (a) Gutmann, V. Solvent Effects on the Reactivities of Organometallic Compounds. *Coord. Chem. Rev.* 1976, *18*, 225–255. (b) Di Girolamo, D.; Pascual, J.; Aldamasy, M. H.; Iqbal, Z.; Li, G.; Radicchi, E.; Li, M.; Turren-Cruz, S.-H.; Nasti, G.; Dallmann, A.; De Angelis, F.; Abate, A. Solvents for Processing Stable Tin Halide Perovskites. *ACS Energy Lett.* **2021**, *6*, 959–968. (c) Lau, K. W.; Aron, M.-H. H.; Yen, M. H.-J.; Fung, E. Y.; Grzybicki, S.; Matamoros, R.; Curtis, J. C. Solvent, Electrolyte and Solute Shape Effects on Optical Electron Transfer in Mixed-Valence Ruthenium Ammine Dimers. *Inorg. Chim. Acta* **1994**, *226*, 137–143.
7. (a) Poling, B. E.; Prausnitz, J. M.; O'Connell, J. P. *The Properties of Gases and Liquids*, 5th ed.; McGraw-Hill: New York, 2000. (b) National Institute of Standards and Technology (NIST). *NIST Chemistry WebBook, SRD 69, Thermophysical Properties of Fluid Systems*; NIST: Gaithersburg, MD, 2020. (c) Jeon, Y.-J.; Lee, S.; Kang, R.; Kim, J.-E.; Yeo, J.-S.; Lee, S.-H.; Kim, S.-S.; Yun, J.-M.; Kim, D.-Y. Planar Heterojunction Perovskite Solar Cells with Superior Reproducibility. *Sci. Rep.* **2014**, *4*, 6953. (d) Babar, D. G.; Olejnik, R.; Slobodian, P.; Matyas, J. High Sensitivity Sensor Development for Hexamethylphosphoramide by Polyaniline Coated

Polyurethane Membrane Using Resistivity Assessment Technique. *Measurement* **2016**, *89*, 72–77. (e) Li, X.; Jiang, Y.; Han, G.; Deng, D. Investigation of the Solubilities of Carbon Dioxide in Some Low Volatile Solvents and Their Thermodynamic Properties. *J. Chem. Eng. Data* **2016**, *61*, 1254–1261. (f) Schackmar, F.; Laufer, F.; Singh, R.; Farag, A.; Eggers, H.; Gharibzadeh, S.; Nejand, B. A.; Lemmer, U.; Hernandez-Sosa, G.; Paetzold, U. W. In Situ Process Monitoring and Multichannel Imaging for Vacuum-Assisted Growth Control of Inkjet-Printed and Blade-Coated Perovskite Thin-Films. *Adv. Mater. Technol.* **2023**, *8*, 2201331.

8. Frisch, M. J.; Trucks, G. W.; Schlegel, H. B.; Scuseria, G. E.; Robb, M. A.; Cheeseman, J. R.; Scalmani, G.; Barone, V.; Petersson, G. A.; Nakatsuji, H.; Li, X.; Caricato, M.; Marenich, A. V.; Bloino, J.; Janesko, B. G.; Gomperts, R.; Mennucci, B.; Hratchian, H. P.; Ortiz, J. V.; Izmaylov, A. F.; Sonnenberg, J. L.; Williams-Young, D.; Ding, F.; Lipparini, F.; Egidi, F.; Goings, J.; Peng, B.; Petrone, A.; Henderson, T.; Ranasinghe, D.; Zakrzewski, V. G.; Gao, J.; Rega, N.; Zheng, G.; Liang, W.; Hada, M.; Ehara, M.; Toyota, K.; Fukuda, R.; Hasegawa, J.; Ishida, M.; Nakajima, T.; Honda, Y.; Kitao, O.; Nakai, H.; Vreven, T.; Throssell, K.; Montgomery, J. A., Jr.; Peralta, J. E.; Ogliaro, F.; Bearpark, M. J.; Heyd, J. J.; Brothers, E. N.; Kudin, K. N.; Staroverov, V. N.; Keith, T. A.; Kobayashi, R.; Normand, J.; Raghavachari, K.; Rendell, A. P.; Burant, J. C.; Iyengar, S. S.; Tomasi, J.; Cossi, M.; Millam, J. M.; Klene, M.; Adamo, C.; Cammi, R.; Ochterski, J. W.; Martin, R. L.; Morokuma, K.; Farkas, O.; Foresman, J. B.; Fox, D. J.
   Gaussian 16, Revision C.01; Gaussian, Inc.: Wallingford, CT, 2016.
9. Hamill, J. C.; Romiluyi, O.; Thomas, S. A.; Cetola, J.; Schwartz, J.; Toney, M. F.; Clancy, P.; Loo, Y.-L. Sulfur-Donor Solvents Strongly Coordinate Pb^{2+} in Hybrid Organic–Inorganic Perovskite Precursor Solutions. *J. Phys. Chem. C* **2020**, *124*, 14496–14502.
10. Nasti, G.; Aldamasy, M. H.; Flatken, M. A.; Musto, P.; Matczak, P.; Dallmann, A.; Hoell, A.; Musiienko, A.; Hempel, H.; Aktas, E.; Di Girolamo, D.; Pascual, J.; Li, G.; Li, M.; Mercaldo, L. V.; De Veneri, P.; Abate, A. Pyridine Controlled Tin Perovskite Crystallization. *ACS Energy Lett.* **2022**, *7*, 3197–3203.
11. (a) Mech, P.; Bogunia, M.; Nowacki, A.; Makowski, M. Calculations of pK_a Values of Selected Pyridinium and Its N Oxide Ions in Water and Acetonitrile. *J. Phys. Chem. A* **2020**, *124*, 538–551. (b) Razali, M.; Kim, J. F.; Attfield, M.; Budd, P. M.; Drioli, E.; Lee, Y. M.; Szekely, G. Sustainable Wastewater Treatment and Recycling in Membrane Manufacturing. *Green Chem.* **2015**, *17*, 5196–5205. (c) Lenarcik, B.; Ojczenasz, P. The Influence of the Size and Position of the Alkyl Groups in Alkylimidazole Molecules on Their Acid-Base Properties. *J. Heterocycl. Chem.* **2002**, *39*, 287–290. (d) Groshens, T. J.; Hollins, R. A. New Chemical Hydrogen Storage Materials Exploiting the Self-Sustaining Thermal Decomposition of Guanidinium Borohydride. *Chem. Commun.* **2009**, *21*, 3089–3091. (e) Rodima, T.; Kaljurand,

I.; Pihl, A.; Mäemets, V.; Leito, I.; Koppel, I. A.
Acid–Base Equilibria in Nonpolar Media. 2. Self-Consistent Basicity Scale in THF Solution Ranging from 2-Methoxypyridine to EtP1(pyrr) Phosphazene. *J. Org. Chem.* **2002**, *67*, 1873–1881.

12. Zhang, M.; Lyu, M.; Yun, J.-H.; Noori, M.; Zhou, X.; Cooling, N. A.; Wang, Q.; Yu, H.; Dastoor, P. C.; Wang, L. Low-Temperature Processed Solar Cells with Formamidinium Tin Halide Perovskite/Fullerene Heterojunctions. *Nano Res.* **2016**, *9*, 1570–1577.
13. Song, D.; Narra, S.; Li, M.-Y.; Lin, J.-S.; Diau, E. W.-G. Interfacial Engineering with a Hole-Selective Self-Assembled Monolayer for Tin Perovskite Solar Cells via a Two-Step Fabrication. *ACS Energy Lett.* **2021**, *6*, 4179–4186.
14. Afraj, S. N.; Kuan, C.; Lin, J.; Ni, J.; Velusamy, A.; Chen, M.; Diau, E. W. Quinoxaline-Based X-Shaped Sensitizers as Self-Assembled Monolayer for Tin Perovskite Solar Cells. *Adv. Funct. Mater.* **2023**, *33*, 2213939.
15. Song, D.; Tseng, H.-Y.; Narra, S.; Tsai, I.-H.; Diau, E. W.-G. Solvent Engineering for Triple Cationic ITO-Based Mesoscopic Tin Perovskite Solar Cells. *Chem. Eng. J.* **2023**, *464*, 142635.
16. Aktas, E.; Poli, I.; Ponti, C.; Li, G.; Olivati, A.; Girolamo, D. D.; Alharthi, F. A.; Li, M.; Palomares, E.; Petrozza, A.; Abate, A. One-Step Solution Deposition of Tin-Perovskite onto a Self-Assembled Monolayer with a DMSO-Free Solvent System. *ACS Energy Lett.* **2023**, *8*, 5170–5174.
17. Song, D.; Ramakrishnan, S.; Zhang, Y.; Yu, Q. Mixed Self-Assembled Monolayers for High-Photovoltage Tin Perovskite Solar Cells. *ACS Energy Lett.* **2024**, *9*, 1466–1472.
18. Afraj, S. N.; Kuan, C.; Cheng, H.; Wang, Y.; Liu, C.; Shih, Y.; Lin, J.; Tsai, Y.; Chen, M.; Diau, E. W. Triphenylamine-Based Y-Shaped Self-Assembled Monolayers for Efficient Tin Perovskite Solar Cells. *Small* **2025**, *21*, 2408638.
19. Huang, J.; Abdel-Shakour, M.; Zhang, S.; Pan, Y.; Wei, X.; Liu, T.; Xiao, H.; Wang, J.; Meng, X. Phytic Acid Dipotassium as a Hole Transport Layer for Stable Tin Halide Perovskite Solar Cells with Tailored Interfacial Chemical Interaction. *Sci. China Chem.* **2025**, https://doi.org/10.1007/s11426-024-2657-8.
20. Jiang, X.; Wang, F.; Wei, Q.; Li, H.; Shang, Y.; Zhou, W.; Wang, C.; Cheng, P.; Chen, Q.; Chen, L.; Ning, Z. Ultra-High Open-Circuit Voltage of Tin Perovskite Solar Cells via an Electron Transporting Layer Design. *Nat. Commun.* **2020**, *11*, 1245.
21. Peng, W.; Mao, K.; Cai, F.; Meng, H.; Zhu, Z.; Li, T.; Yuan, S.; Xu, Z.; Feng, X.; Xu, J.; McGehee, M. D.; Xu, J. Reducing Nonradiative Recombination in Perovskite Solar Cells with a Porous Insulator Contact. *Science* **2023**, *379*, 683-690.

22. Ran, C.; Gao, W.; Li, J.; Xi, J.; Li, L.; Dai, J.; Yang, Y.; Gao, X.; Dong, H.; Jiao, B.; Spanopoulos, I.; Malliakas, C. D.; Hou, X.; Kanatzidis, M. G.; Wu, Z. Conjugated Organic Cations Enable Efficient Self-Healing $FASnI_3$ Solar Cells. *Joule* 2019, *3*, 3072–3087.

23. Chowdhury, T. H.; Kayesh, M. E.; Lee, J.-J.; Matsushita, Y.; Kazaoui, S.; Islam, A. Post-Deposition Vapor Annealing Enables Fabrication of 1 cm^2 Lead-Free Perovskite Solar Cells. *Sol. RRL* **2019**, *3*, 1900245.

24. Ye, T.; Wang, X.; Wang, K.; Ma, S.; Yang, D.; Hou, Y.; Yoon, J.; Wang, K.; Priya, S. Localized Electron Density Engineering for Stabilized B-γ $CsSnI_3$ Based Perovskite Solar Cells with Efficiencies >10%. *ACS Energy Lett.* **2021**, *6*, 1480–1489.

25. Liu, X.; Wu, T.; Luo, X.; Wang, H.; Furue, M.; Bessho, T.; Zhang, Y.; Nakazaki, J.; Segawa, H.; Han, L. Lead-Free Perovskite Solar Cells with over 10% Efficiency and Size 1 cm^2 Enabled by Solvent–Crystallization Regulation in a Two-Step Deposition Method. *ACS Energy Lett.* **2022**, *7*, 425–431.

26. Li, B.; Zhang, C.; Gao, D.; Sun, X.; Zhang, S.; Li, Z.; Gong, J.; Li, S.; Zhu, Z. Suppressing Oxidation at Perovskite–NiOx Interface for Efficient and Stable Tin Perovskite Solar Cells. *Adv. Mater.* **2023**, *e*2309768.

27. Zhang, Z.; Su, Z.; Li, G.; Li, J.; Aldamasy, M. H.; Wu, J.; Wang, C.; Li, Z.; Gao, X.; Li, M.; Abate, A. Improved Air Stability of Tin Halide Perovskite Solar Cells by an n-Type Active Moisture Barrier. *Adv. Funct. Mater.* **2024**, *34*, 202306458.

28. Żuraw, W.; Kubicki, D.; Kudrawiec, R.; Przypis, Ł. Carboxylic Acid-Assisted Synthesis of Tin(II) Iodide: Key for Stable Large-Area Lead-Free Perovskite Solar Cells. *ACS Energy Lett.* **2024**, *9*, 4509–4515.

29. Żuraw, W.; Pacheco, F. A. V.; Sánchez-Diaz, J.; Przypis, Ł.; Escobar, M. A. M.; Almosni, S.; Vescio, G.; Martínez-Pastor, J. P.; Garrido, B.; Kudrawiec, R.; Mora-Seró, I.; Öz, S. Large-Area, Flexible, Lead-Free Sn-Perovskite Solar Modules. *ACS Energy Lett.* **2023**, *8*, 4885–4887.